JOURNAL OF COMPUTATIONAL PHYSICS **137,** 38–78 (1997)
ARTICLE NO. CP975793

Average-State Jacobians and Implicit Methods for Compressible Viscous and Turbulent Flows

P. Batten,* M. A. Leschziner,* and U. C. Goldberg†

**Department of Mechanical Engineering, UMIST, Manchester, United Kingdom;*
†Metacomp Technologies, Inc., USA
E-mail: Paul.Batten@umist.ac.uk

Received November 12, 1996; revised June 19, 1997

Several new implicit schemes for the solution of the compressible Navier–Stokes equations are presented. These methods are derived from a hierarchy of average-state approximate solutions to the Riemann problem, ranging from the Lax–Friedrichs flux to the exact Riemann-solver flux. In contrast to linearised approximations, these methods will (with certain provisos on the signal velocities) enforce the entropy condition and preserve positivity without the need for additional corrections. The hierarchy also encompasses and explains the origin of many other upwind and centred methods, including the space-time scheme (due to Chang) and the more recent FORCE scheme (due to Toro). Based on an analysis of the above hierarchy, attention is focussed on the development of a new implicit scheme using a positivity-preserving version of Toro *et al.*'s HLLC scheme, which is the simplest average-state solver capable of exactly preserving isolated shock, contact, and shear waves. Solutions obtained with this method are essentially indistinguishable from those produced with an exact Riemann solver, whilst convergence to the steady state is the most rapid of all the implicit average-stage schemes considered and directly comparable to that of the unmodified Roe scheme. A new two-step implicit method is applied to various test cases, including turbulent flow with shock/boundary-layer interaction. The new time-stepping scheme is composed of two backward Euler steps, but has twice the convergence rate of the backward Euler scheme and alleviates the convergence problems that are often experienced when employing compressive limiter functions.

1. INTRODUCTION

Ever since the pioneering work of Godunov [11] there has been a steadily increasing interest in upwind methods for approximating the convective fluxes in the

0021-9991/97 $25.00

Euler and Navier–Stokes equations. Much research into numerical methods for compressible fluid flow has focussed on the construction of approximate solutions to the Riemann problem, usually motivated by the fact that exact solutions are expensive to compute. However, there are two further issues which are probably equally significant. First, no route has yet been found to successfully incorporate exact solutions to multidimensional Riemann problems into two- or three-dimensional numerical schemes, and hence, the building blocks of current multidimensional schemes are already linearised approximations. Second, there are obvious advantages in using implicit schemes when solving stiff differential equations (resulting, for example, from the use of transport models of turbulence). In this case, a simple closed-form solution for the numerical flux has the advantage of allowing a rapid evaluation of the analytic Jacobians.

Most of the existing closed-form approximate solutions are capable of giving good solutions to one-dimensional inviscid flow. As experience has grown, however, a number of problems have surfaced in more demanding situations, such as in flows with strong shocks or expansions, or in complex multidimensional flows. Linearised approximate Riemann solvers, in particular, are building up a steady catalogue of failings [10, 28, 21]. There are known entropy corrections[1] for linearised solvers. However, whilst some failings are easily cured, entropy corrections usually have unwanted side-effects, such as rendering the modified solver incapable of recognising isolated discontinuities, which would otherwise have been its main advantage in viscous flow. These difficulties have motivated the investigation of a different class of upwind flux, based on the construction of integral average-state approximations to the Riemann problem.

The concept of average-state approximations was introduced by Harten, Lax, and van Leer [14] in 1983, but actually encompasses many earlier schemes. There is a large hierarchy of numerical fluxes which arise from this approach, all of which may be applied directly to the Euler equations without the need for additional *ad hoc* modifications. Unfortunately, most of these approximations appear to be ill-suited to the implicit solution of the Navier–Stokes equations. One major problem stems from the inability of the simpler flux models to exactly preserve an isolated contact or shear wave. This results in excessive diffusion of boundary layers, yet also poor convergence rates. There is, therefore, a clear requirement to minimise the degree of simplification to a level which does not affect the validity of the underlying physics.

Against this background, much of the present paper is devoted to the construction of an implicit scheme based on the HLLC Riemann solver of Toro *et al.* [34], which contains the most detailed physics of any of the average-stage schemes considered. It transpires that one cannot construct an unconditionally stable implicit HLLC scheme under the assumption that all wave speeds are frozen, as is frequently done in implicit Roe schemes [36–40, 15]. However, by choosing and linearising an estimate for the contact-wave speed, which enforces the equality of the two star pressures, an implicit scheme is obtained which is stable up to infinite CFL numbers

[1] This terminology is widely used, even where the fault has apparently nothing to do with entropy violation.

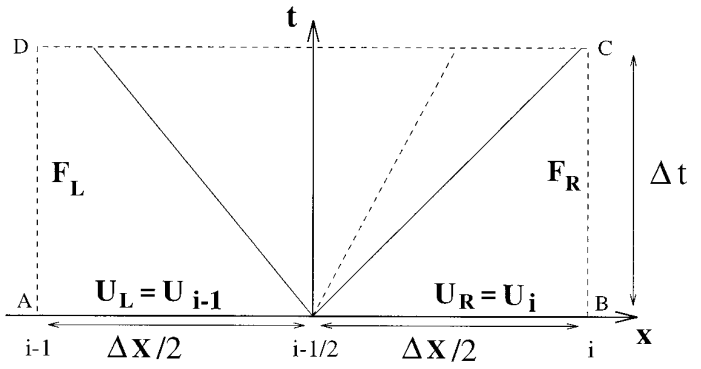

FIG. 1. Region of integration containing the Riemann fan in Godunov's method.

and which is distinguished by the most rapid convergence rate of any of the average-state schemes.

A new two-step time-integration method is developed and applied to various test cases, including turbulent flow with shock/boundary-layer interaction. This two-step method requires no additional storage and may be implemented trivially as two successive backward Euler steps, but has twice the convergence rate of the basic backward Euler scheme and permits convergence to machine zero in situations where compressive limiter functions normally cause the convergence of the backward Euler scheme to stagnate.

2. AVERAGE-STATE APPROXIMATE RIEMANN SOLVERS

The initial-value Riemann problem consists of the interaction of the two semi-infinite states

$$U(x,0) = \begin{cases} U_l & \text{if } x < 0, \\ U_r & \text{if } x \geq 0. \end{cases} \tag{1}$$

The solution is denoted by $R(x/t;\, U_l,\, U_r)$, i.e., depends only on the states U_l, U_r and the ratio x/t. The motivation for solving these wave-interaction problems originated from Godunov's explicit scheme [11], in which piecewise constant data was assumed in each mesh cell and the Riemann problem was solved exactly at the interfaces (see Fig. 1), allowing cell-average values to be updated via an integral average over the cell:

$$U_i^{n+1} = \frac{1}{\Delta x}\int_{i-1/2}^{i} R(x/t, U_{i-1}^n, U_i^n)\, dx + \frac{1}{\Delta x}\int_{i}^{i+1/2} R(x/t, U_i^n, U_{i+1}^n)\, dx. \tag{2}$$

Since the conservation laws

$$\oint [U\, dx - F(U) dt] = 0 \tag{3}$$

must be satisfied over an arbitrary rectangle in x,t space and since the exact Riemann solution satisfies these conservation laws, the above integral can be evaluated over control volume $ABCD$ in Fig. 1 to give the equivalent Godunov update:

$$U_i^{n+1} = U_i^n - \frac{\Delta t}{\Delta x}\{F[R(0, U_{i-1}^n, U_i^n)] - F[R(0, U_i^n, U_{i+1}^n)]\}, \tag{4}$$

where $R(0, U_l, U_r)$ is the solution to the Riemann problem at the interface between states U_l and U_r. Any Godunov-type scheme can be expressed in conservation form, with a numerical flux, $F_{lr}(U_l, U_r)$, determined by applying the integral conservation law (3) over either rectangle $(i - \frac{1}{2}, i) \times (0, \Delta t)$ or, equivalently, rectangle $(i, i + \frac{1}{2}) \times (0, \Delta t)$. The left-hand integral gives

$$F_{lr} = F_l - \frac{1}{\Delta t}\int_{i-1}^{i-1/2} w(\mathrm{x}/\Delta t; U_l, U_r)dx + \frac{\Delta x}{2\Delta t} U_l, \tag{5}$$

where $w(x/t;\ U_{i-1},\ U_i)$ is either the exact or approximate solution to the Riemann problem.

Harten *et al.* [14] proposed various simplifications to the internal structure of the Riemann fan by taking integral averages of the conserved variables over sections of the fan. The most elaborate solver suggested by Harten *et al.* [14] is a two-state approximation in which two integral averages are computed, one from the left-most acoustic wave to the contact and one from the contact to the right-most acoustic wave; see Fig. 2. The details of this scheme are rather cumbersome. However, Toro *et al.* [34] showed that a significant simplification could be made by assuming the particle velocity to be constant across the Riemann fan. Moreover, Batten *et al.* [4] have shown that, with a suitable choice of all wave speeds, Toro *et al.*'s two-state HLLC solver resolves isolated shock and contact/shear waves exactly and is positively conservative in the definition of Einfeldt *et al.* [10], which implies that initially positive densities and pressures are preserved in the internal structure of the Riemann fan. This version of the HLLC flux is defined by

$$F_{HLLC} = \begin{cases} F_l & \text{if } S_L > 0 \\ F(U_l^*) & \text{if } S_L \le 0 < S_M \\ F(U_r^*) & \text{if } S_M \le 0 \le S_R \\ F_r & \text{if } S_R < 0, \end{cases} \tag{6}$$

where

$$U_l^* = \begin{bmatrix} \rho_l^* \\ (\rho u)_l^* \\ (\rho v)_l^* \\ (\rho w)_l^* \\ e_l^* \end{bmatrix} = \Omega_l \begin{bmatrix} \rho_l(S_L - q_l) \\ (S_L - q_l)(\rho u)_l + (p^* - p_l)n_x \\ (S_L - q_l)(\rho v)_l + (p^* - p_l)n_y \\ (S_L - q_l)(\rho w)_l + (p^* - p_l)n_z \\ (S_L - q_l)e_l - p_l q_l + p^* S_M \end{bmatrix}, \tag{7}$$

$$U_r^* = \begin{bmatrix} \rho_r^* \\ (\rho u)_r^* \\ (\rho v)_r^* \\ (\rho w)_r^* \\ e_r^* \end{bmatrix} = \Omega_r \begin{bmatrix} \rho_r(S_R - q_r) \\ (S_R - q_r)(\rho u)_r + (p^* - p_r)n_x \\ (S_R - q_r)(\rho v)_r + (p^* - p_r)n_y \\ (S_R - q_r)(\rho w)_r + (p^* - p_r)n_z \\ (S_R - q_r)e_r - p_r q_r + p^* S_M \end{bmatrix}, \tag{8}$$

$$F_l^* \equiv F(U_l^*) = \begin{bmatrix} \rho_l^* S_M \\ (\rho u)_l^* S_M + p^* n_x \\ (\rho v)_l^* S_M + p^* n_y \\ (\rho w)_l^* S_M + p^* n_z \\ (e_l^* + p^*) S_M \end{bmatrix}, \quad F_r^* \equiv F(U_r^*) = \begin{bmatrix} \rho_r^* S_M \\ (\rho u)_r^* S_M + p^* n_x \\ (\rho v)_r^* S_M + p^* n_y \\ (\rho w)_r^* S_M + p^* n_z \\ (e_r^* + p^*) S_M \end{bmatrix}, \tag{9}$$

$$\Omega_l \equiv (S_L - S_m)^{-1}, \quad \Omega_r \equiv (S_R - S_M)^{-1}, \tag{10}$$

$$p^* = \rho_l(q_l - S_L)(q_l - S_M) + p_l = \rho_r(q_r - S_R)(q_r - S_M) + p_r, \tag{11}$$

and $q \equiv un_x + vn_y + wn_z$, with $[n_x, n_y, n_z]^{\mathrm{T}}$ being the unit vector normal to the interface. S_M is taken from Batten *et al.* [4]:

$$S_M = \frac{\rho_r q_r(S_R - q_r) - \rho_l q_l(S_L - q_l) + p_l - p_r}{\rho_r(S_R - q_r) - \rho_l(S_L - q_l)}, \tag{12}$$

and S_L, S_R are taken from Einfeldt *et al.* [10]:

$$\begin{aligned} S_L &= \min[\lambda_1(U_l), \lambda_1(U^{Roe})], \\ S_R &= \max[\lambda_m(U^{Roe}), \lambda_m(U_r)], \end{aligned} \tag{13}$$

with $\lambda_1(U^{\mathrm{Roe}})$ and $\lambda_m(U^{\mathrm{Roe}})$ being the smallest and largest eigenvalues of the Roe matrix [30].

In some situations, the estimates of the signal velocities, S_L, S_M, and S_R, are not critical. Specific suggestions were made in [7, 10, 34] of how to estimate the acoustic wave speeds, and their performance is observed to be similar in test cases which involve only weak wave interaction. However, differences do arise in more demanding situations. A rather severe example would be the following compression shock-tube problem:

$$\begin{pmatrix} \rho \\ u \\ p \end{pmatrix}_{(x,0)} = \begin{cases} (1, 25, 1/\gamma)^{\mathrm{T}}, & \text{if } x < 0, \\ (1, -25, 1/\gamma)^{\mathrm{T}}, & \text{otherwise}, \end{cases} \tag{14}$$

where the left ($x = -0.5$) and right ($x = 0.5$) ends of the shock-tube correspond to solid walls. Figure 3 shows results for this case at $t = 0.01$, computed using a

first-order scheme with 400 grid points and a CFL number of 0.5 (the exact solution is shown as a solid line). The bursting membrane causes two identical gases to move towards each other at Mach 25, whilst the inward moving rarefaction waves leave, theoretically, vacuum conditions near the two ends of the tube. The original HLLC solver, using any of the wave-speed estimates suggested by Toro *et al.* [34] or Davis [7], fails in the first few time steps, as do Roe's scheme, Osher's scheme, and many of the popular flux–vector splitting schemes. All the average-state fluxes discussed in this paper are capable of giving quite respectable solutions to the above test case, using wave speeds (13) and, where appropriate, (12). Whilst there may be some questions regarding the application of the Euler equations to a flow where the continuum assumption no longer applies, in practice, the approximation of the vacuum as a state with arbitrarily small pressures and densities seems to give perfectly adequate predictions [25], provided the numerical scheme can cope with such conditions.

Although most applications of engineering interest are not so severe, vacuum or near-vacuum conditions can often occur in initial transients. Furthermore, linearised approximate Riemann solvers are known to fail with negative pressures well before the vacuum state is reached [10]. For the Euler equations, linearised Riemann solvers, such as those due to Roe [30], Toro [32], and Eberle [9], can technically be considered as special cases of the two-state HLL approach, but with one important distinction. In these linearised solvers, all wave speeds are obtained from a single average state—for example, an arithmetic or a square-root average. Wave speeds determined in this manner will, in general, underestimate the true expansion-wave velocity, and in Eulerian schemes this is what leads to negative internal energies and expansion shocks.

One other scheme known to be able to resolve the severe transients of test case (14) is the AUSM scheme of Liou and Steffen [21]. Quite a number of different AUSM schemes have now been proposed, but none of these fall within the current hierarchy of solvers, since the AUSM flux is not derived from any integral-average solution, U^*, consistent with the conservation laws (3).

In theory, the average-state concept can be advanced further by the addition of more waves and states, as indicated in Fig. 2. For example, by considering any expansion wave as a single averaged state, the left and right star states on either side of the contact wave become identical to those in the exact Riemann solution. In some algorithms, such as front-tracking, the expansion wave is deliberately divided further into many small integral-average states so that these can be interpreted and propagated as discontinous fronts. The upper limit of the hierarchy is, of course, the exact Riemann solution, but in recent years there has been much attention focussed on simplified average-state schemes that prove to be equally robust when applied to the Euler equations. One such example is the single-state HLL scheme of Harten *et al.* [14] (see Fig. 2):

$$F_{\mathrm{HLL}} = t_1 F_r + t_2 F_l - t_3 (U_r - U_l), \tag{15}$$

with

$$t_1 = \frac{\min(S_R, 0) - \min(0, S_L)}{S_R - S_L}, \quad t_2 = 1 - t_1, \quad t_3 = \frac{S_R |S_{L|} - S_L |S_R|}{2(S_R - S_L)}, \tag{16}$$

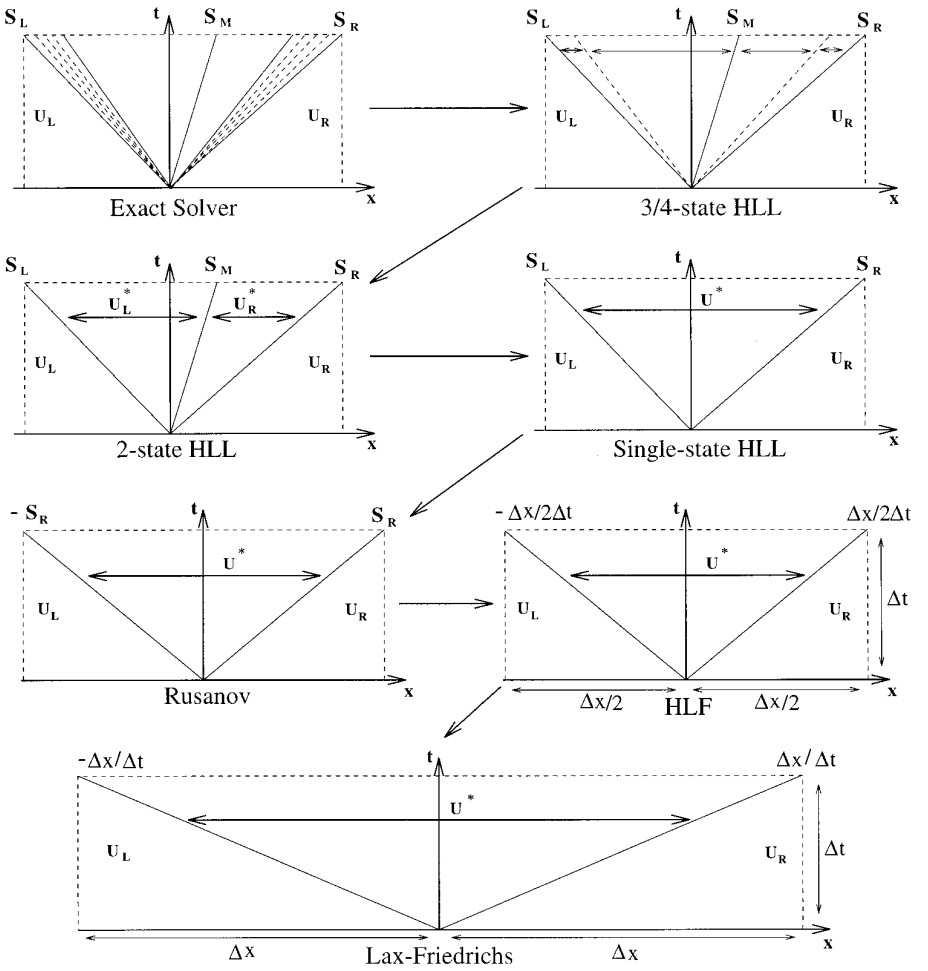

FIG. 2. The hierarchy of average-state Riemann solvers.

where S_L and S_R may again be taken from (13). The HLL flux (15) can resolve isolated shocks as well as an exact Riemann solver and has also been shown to be positively conservative [10] using wave-speed estimates (13). However, it cannot resolve isolated contact/shear waves exactly, and this weakness can be significant for Navier–Stokes computations.

Using algorithm (13) to estimate upper and lower bounds on the true maximum signal speed, λ_m, one can set $S_R = |\lambda_m|$ and $S_L = -S_R$ in the HLL flux formula (15) to arrive at the Rusanov flux (see Davis [7]):

$$F_{\text{Rusanov}} = \frac{1}{2}(F_l + F_r) - \frac{|\lambda_m|}{2}(U_r - U_l). \tag{17}$$

The Rusanov flux has been, and possibly still is, the most popular approach to

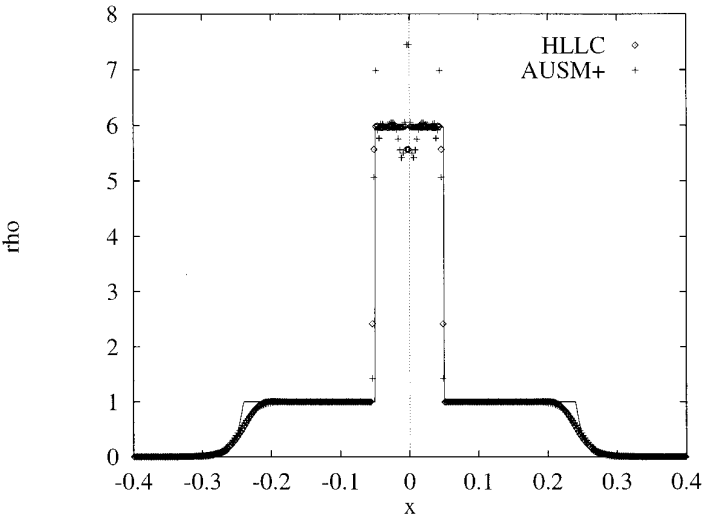

FIG. 3. Mach 25 compression shock-tube problem, 400 grid points, CFL = 0.5.

solving compressible fluid-flow problems and forms the basis of virtually all artificial-viscosity methods. The Roe flux (see Roe [30] and Roe and Pike [31]),

$$F_{\text{Roe}} = \frac{1}{2}(F_l + F_r) - \frac{1}{2} R\Lambda R^{-1}(U_r - U_l) \tag{18}$$

with $\Lambda = \text{Diag}[|\lambda_1|, |\lambda_2|, |\lambda_3|]$, also reduces to (17) if all signal velocities are set equal to $|\lambda_m|$, although it should be noted that the maximum modulus eigenvalue of the Roe matrix may underestimate the true $|\lambda_m|$. Davis [7] has pointed out that the CFL restriction obviates the need to estimate signal velocities through the assumption $|\lambda_m| = \Delta x/\Delta t$, in which case (15) reduces to the Lax–Friedrichs flux:

$$F_{LF} = \frac{1}{2}(F_l + F_r) - \frac{\Delta x}{2\Delta t}(U_r - U_l). \tag{19}$$

Whilst being attractively simple, the Lax–Friedrichs flux is extremely dissipative and produces solutions which are dramatically worse than those computed with the Rusanov flux. Figures 5 and 6 show solutions to Harten's shock-tube problem computed at $t = 0.1$ with various first- and second-order schemes on a uniform one-dimensional mesh of 100 grid points. The results demonstrate that the poor resolution of the Lax–Friedrichs scheme persists even if one uses higher-order methods.

Recently, Chang [6] and Toro [33] have produced two surprisingly accurate shock-capturing schemes that operate without any apparent use of upwinding, Riemann solvers, or even signal velocities. The basic ingredient in both Chang's "space-time" scheme [6] and Toro's "FORCE" scheme [33] is an average-state computed at a location staggered in time and space, as indicated in Fig. 4. Toro [33] suggests using the staggered mesh at the half-time level purely in order to advance the solution

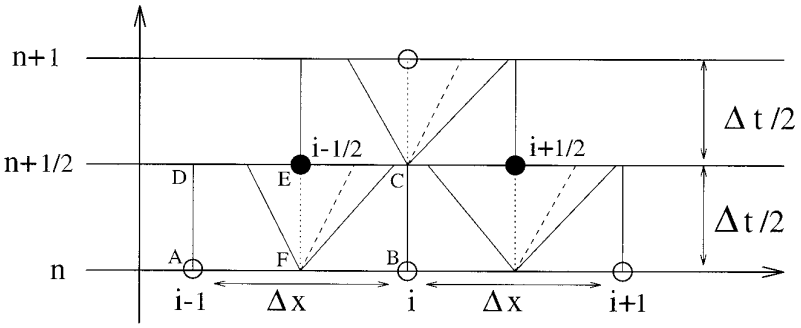

FIG. 4. Staggered mesh used in space-time and FORCE schemes.

to the full time level on the principal mesh, whilst Chang [6] makes no specific distinction between full and half-time levels.

The initial step in the FORCE method is to integrate the conservation laws (3) around the rectangular region *ABCD* in Fig. 4 in order to produce an integral average value at a half-time level, for example,

$$U_{i-1/2}^{n+1/2} = \frac{1}{2}(U_{i-1}^{n} + U_{i}^{n}) + \frac{\Delta t}{2\Delta x}(F_{i-1}^{n} - F_{i}^{n}). \tag{20}$$

Once $U_{i-1/2}^{n+1/2}$ and $U_{i+1/2}^{n+1/2}$ are known, an analogous procedure applied to the staggered grid gives

$$U_{i}^{n+1} = \frac{1}{2}(U_{i-1/2}^{n+1/2} + U_{i+1/2}^{n+1/2}) + \frac{\Delta t}{2\Delta x}(F_{i-1/2}^{n+1/2} - F_{i+1/2}^{n+1/2}). \tag{21}$$

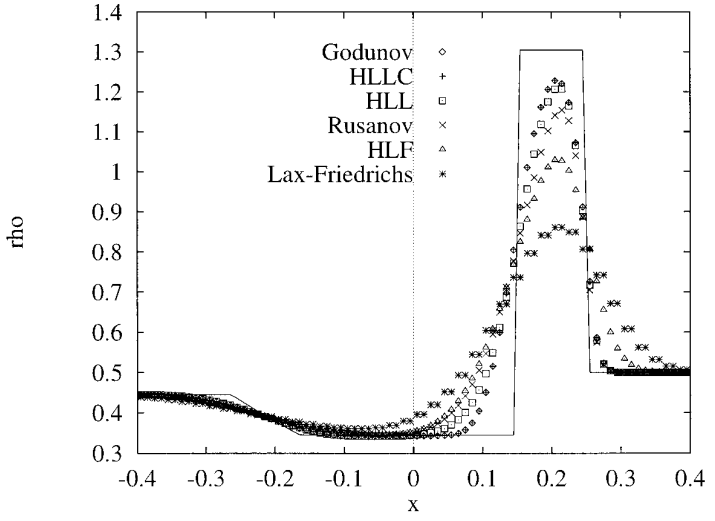

FIG. 5. First-order nonstaggered schemes applied to Harten's shock-tube problem, 100 grid points, CFL = 0.5, $t = 0.1$.

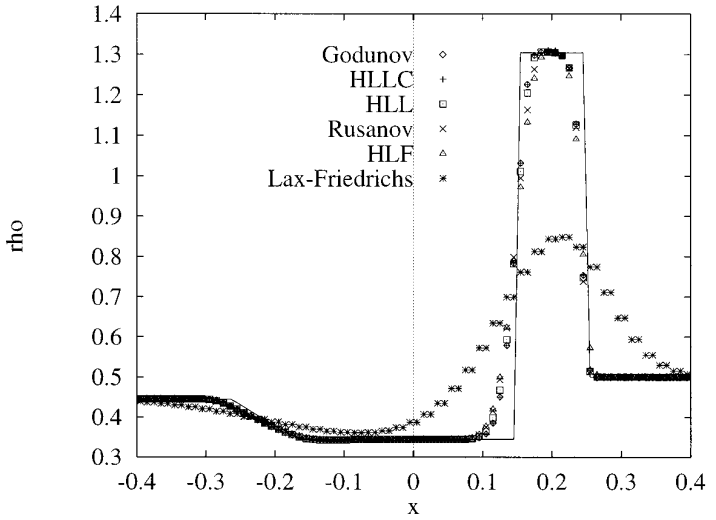

FIG. 6. Second-order nonstaggered Runge–Kutta schemes applied to Harten's shock-tube problem, 100 grid points, CFL = 0.5, $t = 0.1$.

This update can be rewritten in terms of a conservative Godunov-type scheme (4) with the numerical flux,

$$F_{i-1/2}^{\mathrm{FORCE}} = \frac{1}{2}\{F_{i-1/2}^{\mathrm{LF}} + F_{i-1/2}^{\mathrm{RI}}\},$$

which is simply an arithmetic average of the Lax–Friedrichs (F^{LF}) and Richtmyer (F^{RI}) fluxes, where F^{LF} is given by (19) and

$$F_{i-1/2}^{\mathrm{RI}} = F(U_{i-1/2}^{n+1/2}),$$

with $U_{i-1/2}^{n+1/2}$ given by (20). Toro [33] demonstrates that the FORCE scheme applied to the linear advection equation is monotone, provided the CFL number is less than unity.

Chang [6] does not consider U as constant within each cell. Instead, U is reconstructed such that within any "solution element," (i, n), the vector U is taken as

$$U = U_i^n + (U_x)_i^n(x - x_i) + (U_t)_i^n(t - t_n). \tag{22}$$

The solution element (i, n) is considered to range from $[i - \frac{1}{2}, i + \frac{1}{2}]$ and $[n - \frac{1}{2}, n + \frac{1}{2}]$, and, in general, U may be discontinuous at the boundaries of the solution elements. The philosophy of Chang's scheme [6] is to treat space and time equally. Hence, fluxes across vertical lines in Fig. 4 (spatial fluxes) are treated in an identical fashion to fluxes across horizonal lines (temporal fluxes). The scheme is, again, developed by exploiting the fact that the integral form of the conservation law (3) must hold over an arbitrary union of "conservation elements." For example, in Fig. 4:

$$\int_{AFED}[U\,dx - F\,dt] = 0, \tag{23}$$

$$\int_{FBCE}[U\,dx - F\,dt] = 0, \tag{24}$$

$$\int_{ABCD}[U\,dx - F\,dt] = 0. \tag{25}$$

The governing differential equations are assumed to hold over every solution element. For example, in the case of the one-dimensional Euler equations, $(U_t)_i^n = -(F_x)_i^n$. Setting $F_x = (\partial F/\partial U)U_x$, $F_t = (\partial F/\partial U)U_t$, F_x, and, hence, U_t and F_t can be expressed as functions of U and U_x. The only unknowns in Eqs. (23) to (25) are, therefore, the values of U and U_x at the $(i - \frac{1}{2}, n + \frac{1}{2})$ solution element. Since Eqs. (23) plus (24) imply (25), this leaves two equations and two unknowns. Equation (25) may be solved directly for the discrete solution vector at the next half-time level, giving

$$U_{i-1/2}^{n+1/2} = \frac{1}{2}(U_{i-1}^n + U_i^n) + \frac{\Delta t}{2\Delta x}(F_{i-1} - F_i) + \frac{\Delta x}{8}[(U_x)_{i-1}^n - (U_x)_i^n] + \frac{\Delta t^2}{8\Delta x}\left[\left(\frac{\partial F}{\partial U}U_t\right)_{i-1}^n - \left(\frac{\partial F}{\partial U}U_t\right)_i^n\right]. \tag{26}$$

Substituting (26) into either (23) or (24) determines $(U_x)_{i-1/2}^{n+1/2}$. Note that due to the definition of the function U by (22) over the solution element, no interpolation or extrapolation is needed to define the interface fluxes.

The basic space-time scheme described above is neutrally stable and free from dissipation [6]. As a result, the scheme is unsuitable for problems involving discontinuities, such as shocks and contact waves. For this reason, Chang [6] introduces a weighted average form of the derivatives to suppress numerical oscillations:

$$(q_x)_i^n = (q_x^w)_i^n + (2\varepsilon - 1)[(q'_{i+1/2} - q'_{i-1/2})/\Delta x - (q_x)_i^n], \tag{27}$$

where

$$(q_x^w)_i^n = \frac{|a|^\alpha b + |b|^\alpha a}{|a|^\alpha + |b|^\alpha} \tag{28}$$

and α is some positive integer which controls the weighted averaging of the left and right slopes, a and b, defined as

$$a = (q_i^n - q'_{i-1/2})/(\Delta x/2), \quad b = (q'_{i+1/2} - q_i^n)/(\Delta x/2),$$

and

$$q'_{i\pm1/2} = q_{i\pm1/2}^{n-1/2} + (q_t)_{i\pm1/2}^{n-1/2}\frac{\Delta t}{2}. \tag{29}$$

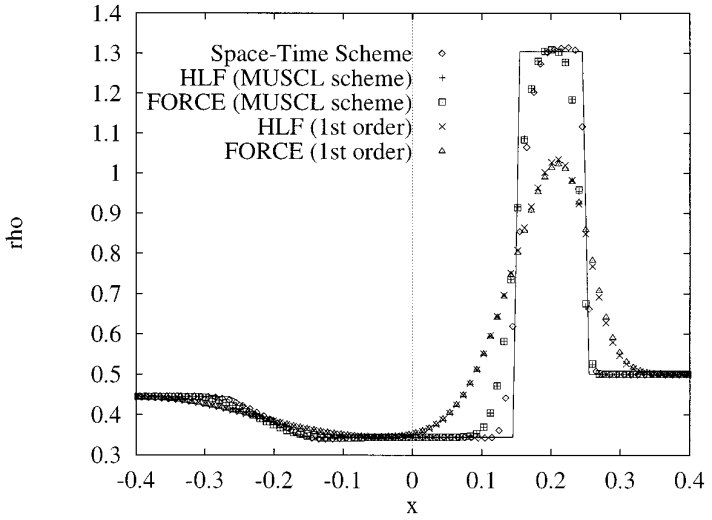

FIG. 7. Space-time scheme and related methods applied to Harten's shock-tube problem, 100 grid points, CFL = 0.5, $t = 0.1$.

Chang [6] refers to the space-time scheme with the components of U_x, defined via (27), as the "$a - \varepsilon$ scheme," in which ε is a parameter which controls the level of artificial dissipation. At least for one-dimensional calculations of the Euler equations, it appears that the solution of evolution equations for the derivatives is an unnecessary overhead, since derivatives obtained via Eq. (23) or (24) are overwritten by any limiter function such as (28) which is subsequently applied in an attempt to preserve monotonicity (note that this scheme is not strictly bounded as there is no guarantee on the monotonicity of the projected solution (29)). Setting $\varepsilon = 0.5$ and $\alpha = 1$, (27) simply reduces to the well-known harmonic-mean slope of van Leer. Using (28) to define each component of U_x, the space-time scheme no longer requires any evolution equation for the spatial derivatives.[2] The result (see Fig. 7) is quite remarkable, considering that the internal details of the Riemann fan are never used and, indeed, are never needed, because the entire Riemann fan is contained within the region of integration.

Part of the reason for this sharp resolution is that the projection (29) makes very efficient use of the extra level of storage. Whilst conventional two-step methods use co-located storage for both levels of data, the two levels of storage in the space-time scheme are staggered in such a way that each provides a type of subcell resolution for the other, since (29) provides solution data *between* current mesh values. Examining data at only one mesh level in the space-time solution (particularly at steady-state!) gives the impression of very sharply captured discontinuities. In fact, solutions produced with this scheme are broadly comparable to conventional MUSCL schemes which use twice the number of mesh points, but with every other mesh point then omitted from the output.

[2] The scheme then also loses its special property of space-time invariance [6]. In practice, this property is lost with the application of any limiter-like device which suppresses numerical oscillations.

In the case where the local gradients within a solution element are zero (the likely effect of employing the slope-limiter (28) near a discontinuity), the evolution equation (26) reduces to (20). Repeating this procedure on the staggered mesh, one can see that the underlying monotone method in the space-time scheme is exactly that of the FORCE scheme.

Whilst mesh staggering does not present much difficulty in one-dimensional problems, in multidimensional calculations it can significantly increase programming overheads. Therefore, this integral-averaging procedure in the first-order space-time or FORCE scheme is re-interpreted for a conventional, nonstaggered mesh, by taking an integral over half of the rectangular domain containing the Riemann fan (see Fig. 1) to construct an average-state approximation to the interface flux via Harten and Lax's formula (5). Integrating (3) over rectangle ABCD in Fig. 1 gives

$$u_{i-1/2}^{n+1} = \frac{1}{2}(U_r + U_l) - \frac{\Delta t}{\Delta x}(F_r - F_l). \tag{30}$$

Substituting (30) into (5) gives

$$F_{\mathrm{HLF}} = \frac{1}{2}(F_l + F_r) - \frac{\Delta x}{4\Delta t}(U_r - U_l). \tag{31}$$

The above numerical flux is readily recognised as being associated with the average-state Riemann solvers. Thus, flux (31) is just the HLL flux (15), with $S_R = \Delta x/2\Delta t$ and $S_L = -S_R$, which corresponds to maximum and minimum bounds for the signal velocities within a CFL restriction of 0.5. Since the dissipation term in this flux is exactly one-half of that in the Lax–Friedrichs flux, we refer to (31) as the "half-Lax–Friedrichs" flux or HLF.

Although signal velocities do not appear directly in the HLF, FORCE, or space-time schemes, one can see that bounds are obtained indirectly through the estimate of Δt. Therefore, the choice of time-step is expected to be highly influential on any transient or steady-state solution. In particular, the dissipation in these methods vanishes as $\Delta t \to \infty$, but tends to infinity as $\Delta t \to 0$. Required conditions for positivity on the Lax–Friedrichs/HLF schemes can be demonstrated on the linear, scalar wave equation,

$$u_t + a u_x = 0,$$

where a is a constant ($a > 0$), and it is assumed that $u_i^n \geq 0\ \forall i$, and $\Delta t > 0$.

Substituting the Lax–Friedrichs/HLF flux into the forward Euler scheme gives

$$u_i^{n+1} = u_i^n - \frac{\Delta t}{\Delta x}\left\{\frac{1}{2}[f(u_i^n) + f(u_{i+1}^n)] - \frac{\beta \Delta x}{2\Delta t}(u_{i+1}^n - u_i^n)\right.$$

$$\left. - \frac{1}{2}[f(u_{i-1}^n) + f(u_i^n)] + \frac{\beta \Delta x}{2\Delta t}(u_i^n - u_{i-1}^n)\right\},$$

where $\beta = 1$ or $\frac{1}{2}$, corresponding to the Lax–Friedrichs or HLF fluxes, respectively.

This can be rearranged to give

$$u_i^{n+1} = u_i^n - \frac{a\Delta t}{2\Delta x}(u_{i+1}^n - u_{i-1}^n) + \frac{\beta}{2}(u_{i+1}^n - 2u_i^n + u_{i-1}^n) \geq \frac{u_{i+1}^n}{2}\left(\beta - \frac{a\Delta t}{\Delta x}\right).$$

Hence, $u^{n+1} \geq 0$, provided the CFL number, $a\Delta t/\Delta x < \beta$.

Substituting the Lax–Friedrichs/HLF flux into the backward Euler scheme gives

$$(1+\beta)u_i^{n+1} - \frac{u_{i+1}^{n+1}}{2}\left[\beta - \frac{a\Delta t}{\Delta x}\right] - \frac{u_{i-1}^{n+1}}{2}\left[\beta + \frac{a\Delta t}{\Delta x}\right] = u_i^n.$$

This forms a diagonally dominant matrix whose diagonal and off-diagonal elements are respectively positive and negative, provided $a\Delta t/\Delta x < \beta$. Thus, the implicit Lax–Friedrichs and HLF schemes are positivity-preserving only up to the same CFL numbers as their explicit counterparts.

Implicit schemes based directly on the Lax–Friedrichs or HLF fluxes are not, therefore, expected to be of much practical use. One way around this difficulty could be to compute and freeze the dissipation parameter in the HLF flux, $\Delta t/\Delta x$, where Δt would be the value obtained assuming a CFL restriction of 0.5, and then to use a different, larger, time-step in the backward Euler scheme itself. This would, at best, simply amount to an application of the implicit Rusanov scheme. Within the required CFL restriction, however, explicit inviscid-flow calculations using the HLF flux show a signficant improvement over those using Lax–Friedrichs. Figure 6, shows results using the HLF flux at a CFL number of 0.5, with the van Leer limiter (corresponding to slope limiter (28) with $\alpha = 1$, $a = (q_i - q_{i-1})/\Delta x$ and $b = (q_{i+1} - q_i)/\Delta x$) used to compute the limited slope, L, in the TVD Runge–Kutta time-stepping scheme,

$$\overline{U}_i = U_i^n - \frac{\Delta t}{\Delta x}\sum_k F(U_i^n + \mathbf{d}_{ik}.L_i^n, U_k^n + \mathbf{d}_{ki}.L_k^n), \tag{32}$$

$$U_i^{n+1} = \frac{1}{2}\left(U_i^n + \overline{U}_i - \frac{\Delta t}{\Delta x}\sum_k F(\overline{U}_i + \mathbf{d}_{ik}.\overline{L}_i, \overline{U}_k + \mathbf{d}_{ki}.\overline{L}_k)\right), \tag{33}$$

in which k corresponds to $i \pm 1$. Figure 6 shows that the HLF results are comparable to those of the other nonstaggered-grid methods based on the HLLC, HLL, Rusanov or exact Riemann-solver fluxes. Comparisons with the space-time and related schemes are shown in Fig. 7.

It must be reiterated, that in most practical applications, one cannot escape the need to compute at least one signal velocity, because an explicit scheme applied on a fixed mesh requires the choice of Δt. These simple fluxes are discussed here principally to identify their connection to the present hierarchy. Whilst they may perform well for simple one-dimensional Euler flows, their use is not recommended, in general, since they are always less accurate than, and offer little advantage in computational economy over the Rusanov flux.[3]

[3] The Rusanov flux has seen renewed interest recently, appearing under the aliases "local Lax–Friedrichs flux" (see Yee [39]) and "scalar diffusive flux" (see Jameson [17]).

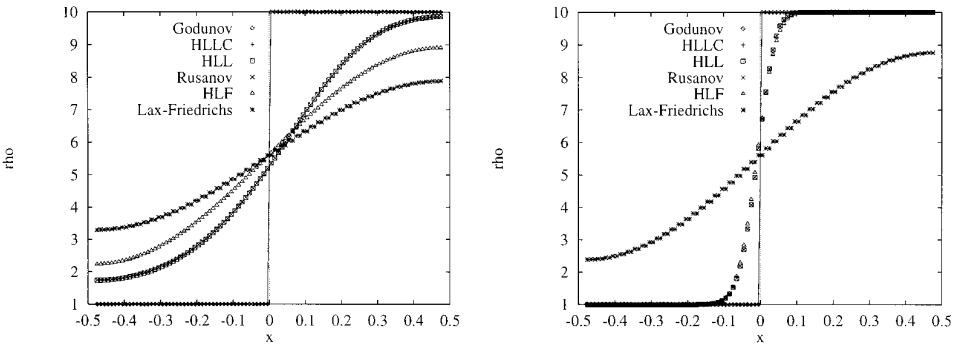

FIG. 8. First- (left) and second-order (right) nonstaggered Runge–Kutta schemes applied to stationary contact problem.

Figures 5 and 6 show that the resolution steadily improves as one moves up the hierarchy of solvers by introducing more waves into the flux model. The simplest flux models estimate only one wave speed, namely that which has the maximum signal speed, and this is used to scale the dissipation applied to all waves. These simple fluxes cannot recognise a wave moving with the $u - c$ characteristic ($u > 0$), since the two states on either side of the slowest-moving acoustic wave in the Riemann fan are averaged, causing upstream-moving or stationary shocks to dissipate. Such schemes will also cause contact waves to diffuse indefinitely, or until checked by boundary conditions or some compressive limiter in the higher-order convective flux, as demonstrated in Fig. 8. In the HLL flux, the other acoustic wave is introduced, and Fig. 5 shows the resulting improvement with respect to the Rusanov and HLF fluxes. Note, however, that contact waves are again diffused indefinitely, and solutions obtained with this scheme in Fig. 8 are indistinguishable from those computed with the Rusanov method. Introducing the contact wave results in a two-state solver, such as HLLC, in which isolated contact or shear waves remain perfectly resolved for all time. In Figs. 5 and 8, the HLLC solutions are indistinguishable from those of the exact Riemann solver.

The importance of preserving isolated contact/shear waves in Navier–Stokes computations can be illustrated by considering a simple boundary layer, where the normal-to-wall pressure gradient and velocity component are nearly zero and the grid is roughly aligned with the wall. Substituting $p_l = p_r = p$ and $q_l = q_r = 0$ into (12) and then into (6), shows that the only nonzero component of the normal-to-wall HLLC flux is the pressure, p. Since the pressure is constant through the boundary layer, it is only the physical diffusion terms which play any role in the flux-balance contribution from the normal-to-wall direction. On the other hand, the HLL, Rusanov, HLF/Lax–Friedrichs, FORCE, and space-time schemes all generate an additional, spurious, convective flux contribution in any property which varies across the boundary layer—for example, shear component of velocity, temperature or density. These schemes will continue diffusing the boundary-layer indefinitely, or until checked by either boundary conditions or some nonlinear effect such as a flux-limiter. Although this diffusion can be reduced to a degree by the

use of compressive limiters, it is unwise to rely on such devices, because one cannot guarantee that the limiter will exactly compensate for the artificial diffusion introduced by the inviscid flux. It is interesting to note that if a scheme *does* resolve the isolated contact/shear problem exactly, then the use of limiters in the normal-to-wall direction has no effect whatsoever.

In the following sections we consider the application of the above fluxes to the implicit solution of the compressible Navier–Stokes equations.

3. A HIERARCHY OF IMPLICIT METHODS

To derive our implicit schemes, inviscid and viscous fluxes are approximated at the new time level via the truncated Taylor expansion,

$$F^{n+1} \approx F^n + \left(\frac{\partial F}{\partial U}\right)^u \delta U.$$

Throughout the remainder of the paper, the superscript $(\,)^n$ will be dropped from the Jacobians whenever this does not cause ambiguity. The implicit semi-discretisation of the mass-averaged Navier–Stokes equations can be written

$$\left[\frac{J}{\Delta t} I - \sum_k \left(\frac{\partial F^v}{\partial U} - \frac{\partial F^c}{\partial U}\right) - J\frac{\partial S^t}{\partial U}\right] \delta U = \sum_k (F^v - F^c)^n + JS_t^n, \tag{34}$$

from which U, the vector of conserved variables, is updated via $U^{n+1} = U^n + \delta U$.

In the above, J is the cell volume, S_t are the source terms (arising, for example, from turbulence-model transport equations), and Σ_k implies a sum over all faces of the control volume. F^c and F^v are the convective- and diffusive-flux vectors, with $\partial F^c/\partial U$ and $\partial F^v/\partial U$ denoting their respective Jacobians.

As a preliminary step, a well-known implicit form of the Roe [30] flux can be obtained by assuming the Roe Jacobian locally frozen (see, for example, Yee [37, 38, 40] or Huang and Coakley [15]), giving

$$F_{\text{Roe}}^{n+1} = \begin{cases} F_l^n + \dfrac{\partial F_l}{\partial U_l}\delta U_l, & \text{if } \lambda_1^n > 0, \\ F_{\text{Roe}}^n + \dfrac{1}{2}\left[\dfrac{\partial F_l}{\partial U_l}\delta U_l + \dfrac{\partial F_r}{\partial U_r}\delta U_r - R|\Lambda|R^{-1}(\delta U_r - \delta U_l)\right], & \text{if } \lambda_1^n \le 0 \le \lambda_3^n, \\ F_r^n + \dfrac{\partial F_r}{\partial U_r}\delta U_r, & \text{if } \lambda_3^n < 0. \end{cases} \tag{35}$$

Strictly, in the subsonic case, there are two terms missing from the above linearisation, corresponding to

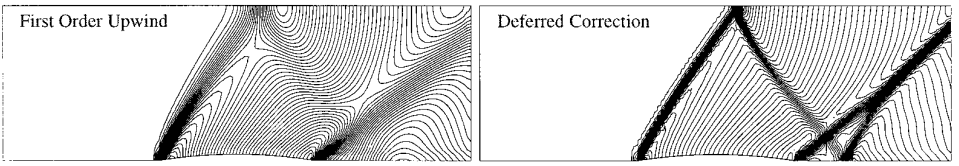

FIG. 9. Mach contours for Mach 1.4 circular-arc bump flow (HLLC).

$$-\frac{1}{2}\frac{\partial}{\partial U_l}\left([R|\Lambda|R^{-1}][U_r^n - U_l^n]\right)\delta U_l - \frac{1}{2}\frac{\partial}{\partial U_r}\left([R|\Lambda|R^{-1}][U_r^n - U_l^n]\right)\delta U_r. \quad (36)$$

Flux (35) with the addition of terms (36) will be referred to as the fully linearised Roe flux. These additional terms may be obtained via repeated application of the product rule, which involves some tedious algebra, but no additional square roots.

Since all these upwind fluxes are only piece-wise differentiable, neither of the above two linearisations will be valid in situations where the wave speeds vary dramatically over one time-step. Eigenvalues can change sign within a single step near sonic points or regions of reverse-flow, and thus it usually proves necessary to start calculations with a CFL number close to unity and to increase Δt substantially only after the wave speeds start to settle down. This is true irrespective of whether wave speeds (and eigenvectors) are frozen or linearised.

Convergence histories comparing the above two linearisations in supersonic and subsonic channel flow are shown in Figs. 10 and 15. A slight improvement in convergence rate is observed with the fully linearised form. However, the cost per iteration increases by more than a factor of two. More complex applications could obviously be envisaged, which are so expensive per step that the number of iterations becomes the most important factor. However, within the present numerical framework and for the problems considered herein, there appears to be no benefit gained from the use of the fully linearised form.

In view of this, the strategy adopted in deriving implicit average-state schemes has been to construct the simplest possible method which gives (linear) unconditional

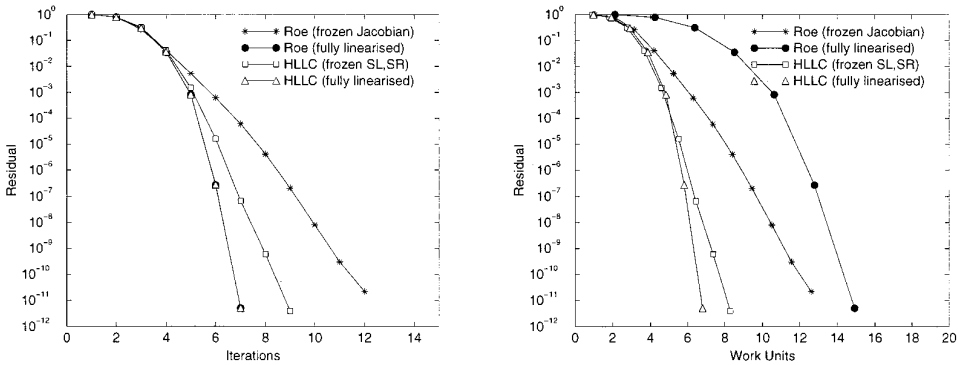

FIG. 10. Convergence histories of first-order backward Euler schemes on supersonic bump flow.

stability. If all wave speeds can be frozen in the construction of the relevant Jacobians, it may be expected that the average-state schemes will result in some extremely simple implicit methods. HLLC turns out to be one exception to this rule. Through the expressions derived from the Rankine–Hugoniot relations (11), the contact-wave speed, S_M (here interpreted also as the average particle velocity between the two acoustic waves), is used to determine both left and right star pressures. The observation that pressure is not discontinuous across the contact wave, i.e.,

$$p_l^* = \rho_l(S_l - q_l)(S_M - q_l) + p_l = p^*, \tag{37}$$

$$p_r^* = \rho_r(S_R - q_r)(S_M - q_r) + p_r = p^*, \tag{38}$$

is enforced only by the choice of contact-wave speed (12). In a linearised implicit scheme with S_M frozen, a disturbance in U_r will cause a disturbance in p_r^* (38), but will have no effect on p_l^* (37). This would imply that, in subsonic flow, downstream disturbances would have no effect whatsoever on the flow upstream. An implicit HLLC scheme with frozen wave speeds could not, therefore, propagate an acoustic wave upstream in subsonic flow any faster than an explicit method. Therefore, the star pressures must be allowed to respond to both upstream and downstream perturbations; hence the expression for the contact-wave velocity must be linearised.

The implicit form of the HLLC flux (6) is then given by

$$F_{\mathrm{HLLC}}^{n+1} = \begin{cases} F_l^n + \dfrac{\partial F_l}{\partial U_l}\delta U_l, & \text{if } S_L^n > 0, \\ (F_l^*)^n + \dfrac{\partial F_l^*}{\partial U_l}\delta U_l + \dfrac{\partial F_l^*}{\partial U_r}\delta U_r, & \text{if } S_L^n \le 0 < S_M^n, \\ (F_r^*)^n + \dfrac{\partial F_r^*}{\partial U_l}\delta U_l + \dfrac{\partial F_r^*}{\partial U_r}\delta U_r, & \text{if } S_M^n \le 0 \le S_R^n, \\ F_r^n + \dfrac{\partial F_r}{\partial U_r}\delta U_r, & \text{if } S_R^n < 0. \end{cases} \tag{39}$$

The supersonic-flow case is again trivial. In the subsonic case, the relevant HLLC Jacobians are given by

$$\frac{\partial F_l^*}{\partial U_l} = \begin{bmatrix} \left(\dfrac{\partial \rho_l^*}{\partial U_l}\right)^{\mathrm{T}} S_M^n + \left(\dfrac{\partial S_M}{\partial U_l}\right)^{\mathrm{T}} \rho_l^* \\ \left(\dfrac{\partial (\rho u)_l^*}{\partial U_l}\right)^{\mathrm{T}} S_M^n + \left(\dfrac{\partial S_M}{\partial U_l}\right)^{\mathrm{T}} (\rho u)_l^* + \left(\dfrac{\partial p^*}{\partial U_l}\right)^{\mathrm{T}} n_x \\ \left(\dfrac{\partial (\rho v)_l^*}{\partial U_l}\right)^{\mathrm{T}} S_M^n + \left(\dfrac{\partial S_M}{\partial U_l}\right)^{\mathrm{T}} (\rho v)_l^* + \left(\dfrac{\partial p^*}{\partial U_l}\right)^{\mathrm{T}} n_y \\ \left(\dfrac{\partial (\rho w)_l^*}{\partial U_l}\right)^{\mathrm{T}} S_M^n + \left(\dfrac{\partial S_M}{\partial U_l}\right)^{\mathrm{T}} (\rho w)_l^* + \left(\dfrac{\partial p^*}{\partial U_l}\right)^{\mathrm{T}} n_z \\ \left(\dfrac{\partial e_l^*}{\partial U_l} + \dfrac{\partial p^*}{\partial U_l}\right)^{\mathrm{T}} S_M^n + (e_l^* + p^*)\left(\dfrac{\partial S_M}{\partial U_l}\right)^{\mathrm{T}} \end{bmatrix} \tag{40}$$

and

$$\frac{\partial F_l^*}{\partial U_r} = \begin{bmatrix} \left(\frac{\partial \rho_l^*}{\partial U_r}\right)^{\mathrm{T}} S_M^n + \left(\frac{\partial S_M}{\partial U_r}\right)^{\mathrm{T}} \rho_l^* \\ \left(\frac{\partial (\rho u)_l^*}{\partial U_r}\right)^{\mathrm{T}} S_M^n + \left(\frac{\partial S_M}{\partial U_r}\right)^{\mathrm{T}} (\rho u)_l^* + \left(\frac{\partial p^*}{\partial U_r}\right)^{\mathrm{T}} n_x \\ \left(\frac{\partial (\rho v)_l^*}{\partial U_r}\right)^{\mathrm{T}} S_M^n + \left(\frac{\partial S_M}{\partial U_r}\right)^{\mathrm{T}} (\rho v)_l^* + \left(\frac{\partial p^*}{\partial U_r}\right)^{\mathrm{T}} n_y \\ \left(\frac{\partial (\rho w)_l^*}{\partial U_r}\right)^{\mathrm{T}} S_M^n + \left(\frac{\partial S_M}{\partial U_r}\right)^{\mathrm{T}} (\rho w)_l^* + \left(\frac{\partial p^*}{\partial U_r}\right)^{\mathrm{T}} n_z \\ \left(\frac{\partial e_l^*}{\partial U_r} + \frac{\partial p^*}{\partial U_r}\right)^{\mathrm{T}} S_M^n + (e_l^* + p^*) \left(\frac{\partial S_M}{\partial U_r}\right)^{\mathrm{T}} \end{bmatrix} \tag{41}$$

Fortunately, these derivatives can be computed in a relatively straightforward manner if the vectors $\partial S_M/\partial U_l$, $\partial S_M/\partial U_r$, $\partial p^*/\partial U_l$, and $\partial p^*/\partial U_r$ are computed and stored in advance. One can simplify this task by exploiting the symmetry property of S_M (12) with respect to p^*. The only U_l terms which appear in p_r^* (38) and the only U_r terms which appear in p_l^* (37) are those in S_M. Hence, in each case, one can choose to differentiate the simpler of the two expressions. The S_M derivatives are first computed from

$$\frac{\partial S_M}{\partial U_l} = \tilde{\rho}^{-1} \begin{bmatrix} -q_l^2 + \psi_l(\gamma - 1)/2 + S_M S_L \\ n_x(2q_l - S_L - S_M) + (1 - \gamma)u_l \\ n_y(2q_l - S_L - S_M) + (1 - \gamma)v_l \\ n_z(2q_l - S_L - S_M) + (1 - \gamma)w_l \\ \gamma - 1 \end{bmatrix}, \tag{42}$$

$$\frac{\partial S_M}{\partial U_r} = \tilde{\rho}^{-1} \begin{bmatrix} q_r^2 - \psi_r(\gamma - 1)/2 - S_M S_R \\ n_x(S_R + S_M - 2q_r) - (1 - \gamma)u_r \\ n_y(S_R + S_M - 2q_r) - (1 - \gamma)v_r \\ n_z(S_R + S_M - 2q_r) - (1 - \gamma)w_r \\ 1 - \gamma \end{bmatrix}, \tag{43}$$

with $\psi \equiv u^2 + v^2 + w^2$ and $\tilde{\rho} \equiv \rho_r(S_R - q_r) - \rho_l(S_L - q_l)$. Differentiating (37) with respect to U_r and (38) with respect to U_l then gives

$$\frac{\partial p^*}{\partial U_l} = \rho_r(S_R - q_r) \frac{\partial S_M}{\partial U_l}, \tag{44}$$

$$\frac{\partial p^*}{\partial U_r} = \rho_l (S_L - q_l) \frac{\partial S_M}{\partial U_r}. \tag{45}$$

The remaining terms in (40) and (41) are

$$\frac{\partial \rho_l^*}{\partial U_l} = \Omega_l \begin{bmatrix} S_L \\ -n_x \\ -n_y \\ -n_z \\ 0 \end{bmatrix} + \Omega_l \rho_l^* \frac{\partial S_M}{\partial U_l}, \tag{46}$$

$$\frac{\partial \rho_l^*}{\partial U_r} = \Omega_l \rho_l^* \frac{\partial S_M}{\partial U_r}, \tag{46a}$$

$$\frac{\partial (\rho u)_l^*}{\partial U_l} = \Omega_l \begin{bmatrix} q_l u_l - n_x \psi_l (\gamma - 1)/2 \\ S_L - q_l + n_x (\gamma - 2) u_l \\ -u_l n_y + n_x (\gamma - 1) v_l \\ -u_l n_z + n_x (\gamma - 1) w_l \\ (1 - \gamma) n_x \end{bmatrix} + \Omega_l \left(n_x \frac{\partial p^*}{\partial U_l} + (\rho u)_l^* \frac{\partial S_M}{\partial U_l} \right), \tag{47}$$

$$\frac{\partial (\rho u)_l^*}{\partial U_r} = \Omega_l \left(n_x \frac{\partial p^*}{\partial U_r} + (\rho u)_l^* \frac{\partial S_M}{\partial U_r} \right), \tag{48}$$

$$\frac{\partial (\rho v)_l^*}{\partial U_l} = \Omega_l \begin{bmatrix} q_l v_l - n_y \psi_l (\gamma - 1)/2 \\ -v_l n_x + n_y (\gamma - 1) u_l \\ S_L - q_l + n_y (\gamma - 2) v_l \\ -v_l n_z + n_y (\gamma - 1) w_l \\ (1 - \gamma) n_y \end{bmatrix} + \Omega_l \left(n_y \frac{\partial p^*}{\partial U_l} + (\rho v)_l^* \frac{\partial S_M}{\partial U_l} \right), \tag{49}$$

$$\frac{\partial (\rho v)_l^*}{\partial U_r} = \Omega_l \left(n_y \frac{\partial p^*}{\partial U_r} + (\rho v)_l^* \frac{\partial S_M}{\partial U_r} \right), \tag{50}$$

$$\frac{\partial (\rho w)_l^*}{\partial U_l} = \Omega_l \begin{bmatrix} q_l w_l - n_z \psi_l (\gamma - 1)/2 \\ -w_l n_x + n_z (\gamma - 1) u_l \\ -w_l n_y + n_z (\gamma - 1) v_l \\ S_L - q_l + n_z (\gamma - 2) w_l \\ (1 - \gamma) n_z \end{bmatrix} + \Omega_l \left(n_z \frac{\partial p^*}{\partial U_l} + (\rho w)_l^* \frac{\partial S_M}{\partial U_l} \right), \tag{51}$$

$$\frac{\partial(\rho w)_l^*}{\partial U_r} = \Omega_l \left(n_z \frac{\partial p^*}{\partial U_r} + (\rho w)_l^* \frac{\partial S_M}{\partial U_r} \right), \tag{52}$$

$$\frac{\partial e_l^*}{\partial U_l} = \Omega_l \begin{bmatrix} (e_l + p_l) q_l / \rho_l - q_l \psi_l (\gamma - 1)/2 \\ -n_x (e_l + p_l)/\rho_l + (\gamma - 1) u_l q_l \\ -n_y (e_l + p_l)/\rho_l + (\gamma - 1) v_l q_l \\ -n_z (e_l + p_l)/\rho_l + (\gamma - 1) w_l q_l \\ S_L - q_l \gamma \end{bmatrix} + \Omega_l \left(\frac{\partial p^*}{\partial U_l} S_M + (p^* + e_l^*) \frac{\partial S_M}{\partial U_l} \right), \tag{53}$$

$$\frac{\partial e_l^*}{\partial U_r} = \Omega_l \left(\frac{\partial p^*}{\partial U_r} S_M + (p^* + e_l^*) \frac{\partial S_M}{\partial U_r} \right). \tag{54}$$

In the case where $S_M^n < 0$, the relevant Jacobians are obtained by simply interchanging subscripts $l \leftrightarrow r$ and $L \leftrightarrow R$ in (46) through (54). This completes the definition of the frozen acoustic wave-speed version of the implicit HLLC flux.

In view of the previous discussion on the various possible linearisations of the Roe flux, the fully linearised form of the HLLC flux will also be considered for comparison. In this case, the derivatives, $\partial S_L/\partial U_l$, $\partial S_L/\partial U_r$, $\partial S_R/\partial U_l$, and $\partial S_R/\partial U_r$ are also required. Note that the acoustic wave speeds are again only piecewise differentiable, the appropriate function being defined by the explicitly determined bound on the signal velocities (13). The derivatives of S_M and U^* above must now be appended with the additional terms,

$$\frac{\partial S_M}{\partial U_l} = \frac{\partial S_M}{\partial U_l} + \tilde{\rho}^{-1} \left[\rho_r (q_r - S_M) \frac{\partial S_R}{\partial U_l} - \rho_l (q_l - S_M) \frac{\partial S_L}{\partial U_l} \right], \tag{55}$$

$$\frac{\partial S_M}{\partial U_r} = \frac{\partial S_M}{\partial U_r} + \tilde{\rho}^{-1} \left[\rho_r (q_r - S_M) \frac{\partial S_R}{\partial U_r} - \rho_l (q_l - S_M) \frac{\partial S_L}{\partial U_r} \right], \tag{56}$$

$$\frac{\partial p^*}{\partial U_l} = \frac{\partial p^*}{\partial U_l} + \rho_r (S_M - q_r) \frac{\partial S_R}{\partial U_l}, \tag{57}$$

$$\frac{\partial p^*}{\partial U_r} = \frac{\partial p^*}{\partial U_r} + \rho_l (S_M - q_l) \frac{\partial S_L}{\partial U_r}, \tag{58}$$

$$\frac{\partial U(i)_l^*}{\partial U_l} = \frac{\partial U(i)_l^*}{\partial U_l} + \Omega_l (U(i)_l - U(i)_l^*) \frac{\partial S_L}{\partial U_l}, \tag{59}$$

$$\frac{\partial U(i)_l^*}{\partial U_r} = \frac{\partial U(i)_l^*}{\partial U_r} + \Omega_l (U(i)_l - U(i)_l^*) \frac{\partial S_L}{\partial U_r}, \tag{60}$$

where $U(i)$ denotes the ith component of vector U. Figures 10 and 15 show comparisons of convergence histories with the two different linearisations in a supersonic and subsonic channel flow. Whilst there is, again, a slightly improved convergence rate using the fully linearised HLLC flux, the extra work required per iteration does not significantly favour this scheme over the simplified form. In view of this,

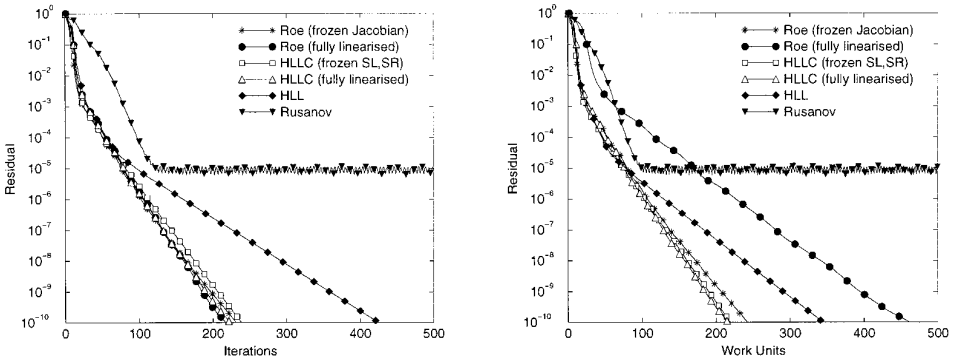

FIG. 11. Convergence histories of deferred correction B2 schemes on supersonic bump flow.

only the simpler, frozen S_L,S_R version will be considered in the remainder of this paper. Due to the very different flux constructions in the Roe and HLLC schemes, the simplified (frozen Jacobian) Roe and simplified (frozen S_L,S_R) HLLC schemes involve very different approximations. Therefore, all subsequent convergence histories are shown in terms of work units as well as numbers of iterations. The remaining average-state schemes require knowledge of only the acoustic wave speeds which may be frozen in each case without loss of stability. Since the aim is to construct the simplest unconditionally stable scheme for each flux, fully linearised versions of the simpler average-state fluxes will not be considered here.

The implicit version of the single-state HLL flux (15) takes a particularly simple form, upon freezing the two acoustic wave speeds, to give

$$F^{n+1}_{\mathrm{HLL}} = F^{n}_{\mathrm{HLL}} + t^n_1 \frac{\partial F_r}{\partial U_r}\,\delta U_r + t^n_2 \frac{\partial F_l}{\partial U_l}\,\delta U_l - t^n_3(\delta U_r - \delta U_l), \tag{61}$$

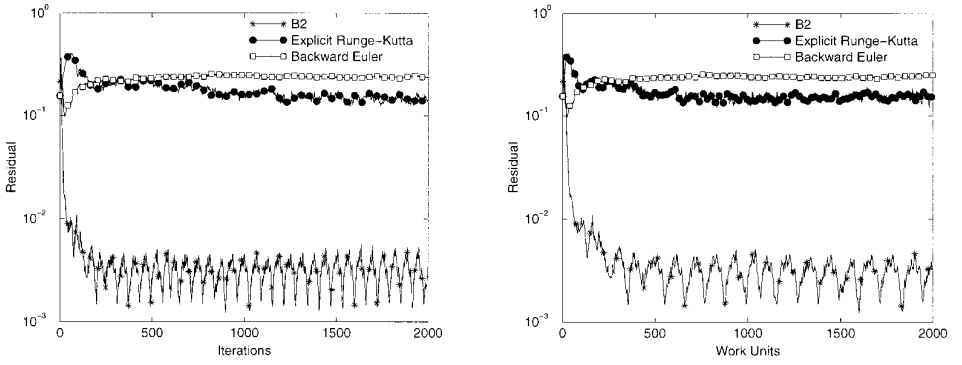

FIG. 12. Supersonic bump flow–convergence histories with SUPERBEE limiter.

where t_1, t_2, and t_3 are given by (16). The implicit Rusanov flux becomes

$$F^{n+1}_{\text{Rusanov}} = F^{n}_{\text{Rusanov}} + \frac{1}{2}\left(\frac{\partial F_r}{\partial U_r}\delta U_r + \frac{\partial F_l}{\partial U_l}\delta U_l\right) - \frac{|\lambda_m|^n}{2}(\delta U_r - \delta U_l), \tag{62}$$

and the implicit Lax–Friedrichs/HLF flux becomes

$$F^{n+1}_{\text{HLF}} = F^{n}_{\text{HLF}} + \frac{1}{2}\left(\frac{\partial F_r}{\partial U_r}\delta U_r + \frac{\partial F_l}{\partial U_l}\delta U_l\right) - \frac{\beta \Delta x}{2\Delta t}(\delta U_r - \delta U_l). \tag{63}$$

The implicit flux (63) has a naturally implied frozen wave speed. However, it was shown in Section 2 that implicit methods based on (63) are not positivity-preserving at CFL numbers larger than β, and we will therefore not give further consideration to either the HLF or the Lax–Friedrichs fluxes.

4. PRESENT NUMERICAL IMPLEMENTATION

4.1. *Mean-Flow Equations*

The starting point for the numerical scheme is a substitution of the linearised convective flux into the backward Euler method:

$$\frac{J\delta U}{\Delta t} = \sum_k (F^v + F^c)^{n+1} + JS_t^{n+1}. \tag{64}$$

$(F^c)^{n+1}$ refers to the implicit convective flux which is approximated via one of the linearisations discussed in the previous section. The viscous flux, $(F^v)^{n+1}$, is discretised via central differences and linearised assuming the laminar viscosity and any (effective isotropic or anisotropic) eddy viscosities are frozen. The latter approximation does not significantly restrict the allowable time-step, since diffusion tends to be an inherently stabilising process. The source terms, S_t^{n+1}, are also treated via central differencing. The linearisation of these terms is discussed in Section 4.2. Once the appropriately linearised terms are substituted into (64), this can be rearranged into the semi-discrete form (34). In practice, we do not use backward Euler time-stepping. A new two-step scheme is proposed in Section 4.3, which is found to give better convergence behaviour in conjunction with higher-order methods.

Higher-order accuracy is achieved using slope-limiting, performed either directly on the conserved variables, or wave-by-wave. Our experience suggests that there is little difference between reconstructions applied to either primitive or conserved variables, provided a check is included in the latter case to exclude the possibility of negative reconstructed pressures. The wave-by-wave (sometimes termed field-by-field) approach decomposes the local solution into contributions from each separate wave, and this can yield an improvement in unsteady flows, particularly when used in conjunction with compressive limiters. In steady flows, where most discontinuities become well separated, the advantages of a wave-by-wave approach are less pronounced. Also, use of wave-by-wave limiting might hinder the present comparisons, because this technique can be applied with Godunov, HLLC, or Roe-type methods, but not with the HLL, Rusanov, or Lax–Friedrichs/HLF schemes,

since these simpler schemes do not provide information on the relative jumps across all waves. Therefore, all higher-order results presented here were computed via conserved-variable reconstruction, using slope-limiters such as (28) applied along coordinate lines as in schemes (32), (33).

There is an open question regarding the optimal choice of implicit operator in higher-order schemes. At large time-steps, discontinuities may travel further than one cell per iteration, and Godunov's theorem implies that a linearised implicit scheme cannot be both monotonicity-preserving and better than first-order accurate. Yee [36] demonstrated that one can maintain TVD solutions at arbitrary time-steps by sacrificing conservation, and this nonconservative linearisation was, in fact, the form adopted by Huang and Coakley [15]. Although use of the δ-form (34) means that such an approximation will not affect the steady state, Yee [38, 40] has shown that the nonconservative linearisation can lead to convergence problems. A fully conservative approach has therefore been adopted here, in which the left-hand-side operator is composed only of contributions from the first-order upwind flux. However, for physically positive quantities, realisability is enforced numerically by the procedure described in Section 4.2.

4.2. *Turbulence-Model Equations*

With the addition of a turbulence model, the total energy becomes the sum of internal, mean-flow kinetic and turbulence energy:

$$e = \rho e_i + \rho(u^2 + v^2 + w^2)/2 + \rho k.$$

Pressures, enthalpies, and all wave speeds need to be modified accordingly in both fluxes and Jacobians. This is straightfoward in the case of any average-state scheme; in the case of any linearised Riemann solver, the eigenvectors also have to be modified to account for the contribution of k to the total energy (see, for example, Barakos and Drikakis [3]). The convective fluxes of any conserved, transported quantity, $\rho\phi$, in the case of HLL, Rusanov, or HLF, extend trivially from the original definitions. The HLLC flux for $\rho\phi$ is again given by (6), where F_l^*, F_r^* are obtained from the conservation laws as

$$F_l^*(\rho\phi) = \rho_l^* \phi_l S_M, \quad F_r^*(\rho\phi) = \rho_r^* \phi_r S_M.$$

The present code is currently being used to validate a range of different turbulence models, including full Reynolds-stress closures. Therefore, a numerical framework has been adopted in which different turbulence models can be easily inserted and modified. Specifically, a fully coupled treatment of the turbulence variables is deliberately avoided. Instead, an uncoupled, implicit equation for any turbulence-related quantity, $\rho\phi$, is derived by considering only diagonal components of the convective, diffusive, and source-term Jacobians. In the case of HLLC, the convection coefficients which contribute to the implicit equation for $\rho\phi$ are

$$\frac{\partial F(\rho\phi)^{\mathrm{HLLC}}}{\partial(\rho\phi)_l} = \max\left[\frac{F(\rho)^{\mathrm{HLLC}}}{\rho_l}, 0\right], \tag{65}$$

$$\frac{\partial F(\rho\phi)^{\mathrm{HLLC}}}{\partial(\rho\phi)_r} = \min\left[\frac{F(\rho)^{\mathrm{HLLC}}}{\rho_r}, 0\right]. \tag{66}$$

Although the turbulence energy can have a weak influence on the mass flux, $F(\rho)^{\mathrm{HLLC}}$, this has been ignored in the implicit part of the operator. This approximation does not affect the converged solution because of the use of the δ-form (34).

Since the higher-order, deferred-correction approach is not necessarily TVD, there is no guarantee that quantities such as turbulence energy will remain positive. Although this procedure cannot guarantee bounded solutions for ϕ for arbitrary time-steps, the weaker, but sufficient condition of positivity-preservation can be achieved for any transported quantity by splitting both convective and diffusive fluxes into

$$F = F_{\mathrm{Implicit}} + F_{\mathrm{Correction}},$$

where F_{Implicit} corresponds to the implicitly treated portion of the fluxes and $F_{\mathrm{Correction}}$ corresponds to any explicitly treated additions. The sum of the flux corrections are treated as a source term and are linearised via the following approach, due to Patankar [27]. The uncoupled, implicit equation for any conserved scalar quantity, $\rho\phi$, may be written as

$$\frac{J[(\rho\phi)^{n+1} - (\rho\phi)^n]}{\Delta t} - \sum f^{n+1} d\mathbf{s} = Js_t + s_c,$$

where $\sum f^{n+1}\, d\mathbf{s}$ denotes the sum of all implicitly discretised fluxes (including diffusion and convection terms), s_t are the source terms arising from the turbulence model, and s_c represents the sources from any deferred-corrections.

Linearising convective and diffusive fluxes and splitting all sources into positive and negative contributions gives

$$\left[\frac{J}{\Delta t} - \sum \frac{\partial f}{\partial(\rho\phi)}\right] \delta(\rho\phi) = \sum f^n + J[s_t^+ + s_t^-] + s_c^+ + s_c^-.$$

Positive source terms are treated explicitly, whilst negative contributions are scaled by $(\rho\phi)^{n+1}/(\rho\phi)^n$ and moved to the left-hand side of the equations. Introducing a small positive constant, $\varepsilon = 10^{-40}$, to prevent division by zero gives

$$\left[\frac{J}{\Delta t} - \sum \frac{\partial f}{\partial(\rho\phi)}\right] \delta(\rho\phi) - \left[\frac{Js_t^- + s_c^-}{(\rho\phi)^n + \varepsilon}\right] (\rho\phi)^{n+1} = \sum f^n + Js_t^+ + s_c^+. \tag{67}$$

To retain the δ form, the term $\left[\frac{Js_t^- + s_c^-}{(\rho\phi)^n + \varepsilon}\right](\rho\phi)^n$ is added to both sides of Eq. (67) to give

$$\left[\frac{J}{\Delta t} - \sum \frac{\partial f}{\partial(\rho\phi)} - \frac{Js_t^- + s_c^-}{(\rho\phi)^n + \varepsilon}\right] \delta(\rho\phi) = \sum f^n + Js_t^+ + s_c^+ + \left[\frac{Js_t^- + s_c^-}{(\rho\phi)^n + \varepsilon}\right] (\rho\phi)^n. \tag{68}$$

In the above form, all flux balance and source terms appear on the right-hand side. However, the small parameter, ε, also appears in the denominator of the s^- terms on both left- and right-hand sides of the equation. One might expect that the $(\rho\phi)^n$ terms on the right-hand side could be cancelled by ignoring this small parameter. However, since it is possible for $\phi \to 0$, this term cannot be ignored, since $(\rho\phi)^n < \varepsilon$ will again lead to small negative values of ϕ in subsequent iterations.

The above procedure has no effect on the converged solution, but it ensures that positivity is preserved on relevant data, such as the normal stresses, turbulence energy, and dissipation rate, even if the turbulence model itself is not strictly realisable. For the test cases considered here, no such procedure was found necessary on any mean-flow equation. In this case, the deferred-correction terms, $\sum_k F_{\text{Correction}}$, were simply treated explicitly.

4.3. *A Two-Step Time-Integration Method*

The use of compressive or moderately compressive limiter functions can often create a flip-flop effect at alternate time steps, which prevents convergence to machine zero. This effect is not associated with physical unsteadiness or turbulence, but is due to the artificial nonlinearity specifically introduced into the discretised convective term to circumvent Godunov's theorem [11] which states that no fixed-stencil scheme can be both monotone and better than first-order accurate.

To improve the convergence behaviour without resorting to more diffusive limiters, a new implicit, temporally first-order scheme has been developed which is subsequently denoted B2:

$$U^{n+1} = U^n + \frac{\Delta t}{2J}\left(\sum_k F^{n+1/2} + \sum_k F^{n+3/2}\right) \tag{69}$$

In regions containing any residual flip-flop effect due to limiter functions, scheme (69) introduces a strong dissipation via the temporal operator. Note that if the backward Euler and B2 schemes both converge to $\sum F^n = 0$, then both converge to the same solution, and the B2 scheme introduces no additional dissipation in the final solution.

The B2 scheme (69) can be implemented as a trivial modification to the backward Euler method and requires no additional storage. Denoting the backward Euler update by

$$\begin{aligned} \delta U &= B1(U^n, \Delta t), \\ U^{n+1} &= U^n + \delta U, \end{aligned} \tag{70}$$

the B2 scheme (69) can be implemented via the following two successive backward Euler steps:

$$\begin{aligned} \delta\overline{U} &= B1(U^n, \Delta t/2), \\ \overline{U} &= U^n + \delta\overline{U}, \end{aligned} \tag{71}$$

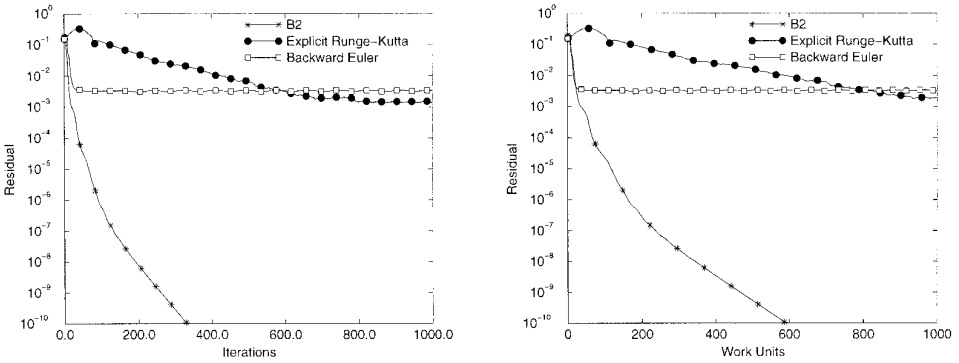

FIG. 13. Supersonic bump flow–convergence histories with van Leer limiter.

$$\delta\tilde{U} = B1(\overline{U}, \Delta t),$$
$$U^{n+1} = \overline{U} + \delta\tilde{U}/2. \tag{72}$$

Figures 12 and 13 show the convergence history for a Mach 1.4 inviscid bump flow (Fig. 9) using the SUPERBEE limiter of Roe and harmonic-mean limiter of van Leer, with various explicit and implicit HLLC schemes. Residuals are also shown versus work units, corresponding to seconds of CPU time on an SGI Indigo 2, R4400 processor. Here, the residual is the normalised sum of the absolute u-momentum flux imbalances.

The explicit Runge–Kutta scheme (32), (33) was applied with a constant local CFL number of 0.6, whilst both implicit schemes used a constant local CFL number of 10^6. It is clear that SUPERBEE causes convergence problems, and this effect has been reported previously by Huang and Coakley [15] who used an implicit Roe scheme. Although none of these SUPERBEE schemes allows convergence to machine zero, the residuals in the B2 scheme are reduced by an additional two orders of magnitude, in comparison with the backward Euler scheme. Even during the early stages of the calculation with van Leer's limiter, where the residuals of the backward Euler method are dropping quite rapidly, the residuals of the B2 scheme reduce at about twice that rate. The B2 scheme converges to 10^{-10}, whilst the residuals of the backward Euler and explicit Runge–Kutta schemes both stagnate at around 10^{-3}. This can often be avoided by using a more diffusive limiter such as MinMod, or by adding fourth-order dissipation or down-wind weighting factors, but the effect of all these approaches is to add dissipation indiscriminately, which inevitably pollutes the final steady-state solution.

The damping in the B2 scheme relates only to the Nyquist frequency associated with the flip-flop of the solution in alternate time-steps; hence a periodic fluctuation at a lower frequency due to error or physical unsteadiness will not necessarily be suppressed. For linear problems, the B2 scheme reduces to the backward Euler scheme.

Whilst the B2 scheme does not cure the underlying cause of convergence difficulties with compressive limiters, it does help to alleviate the symptoms. It is important

to highlight the fact that the residual reported here is the total sum of all absolute u-momentum flux imbalances and not simply the maximum (or average) change in a particular variable. Hence, there is a genuine benefit in terms of the reduction in the level of error achieved in the steady-state discretisation. The flux-imbalance sum also provides a more reliable measure of convergence, because of the possibility of generating spurious steady-state solutions (see Yee and Sweby [41]). In subsequent convergence histories, one iteration is taken to mean one complete backward Euler step or one complete B2 step. Since one B2 iteration involves twice as much effort as one backward Euler iteration, residuals are also shown versus work units. In Section 5, the backward Euler and B2 methods are used to evaluate the relative performance of the various implicit average-state Jacobian schemes on several different test cases.

4.4. *Boundary Conditions*

Implicit schemes can encounter a restrictive CFL-like condition if boundary conditions are not treated in a fully implicit fashion. In the present numerical framework, boundary conditions in both explicit and implicit portions of the scheme are treated consistently by imposing ''ghost'' cells outside the domain. Supersonic inflow and outflow boundaries are treated by fixing and extrapolating all quantities, respectively. Subsonic inflow boundaries are treated either via Riemann invariants [16] or via a reservoir condition in which total temperature and pressure are specified. Subsonic outflow boundaries are treated by imposing a back-pressure, with velocities and temperatures extrapolated. Once the relevant explicit boundary conditions are set on the right-hand side of (34), the equation for any node, i, which falls adjacent to a ghost volume, l, becomes

$$\left(\frac{\Delta t}{J} - \sum_k \frac{\partial F}{\partial U_i} - J\frac{\partial S_t}{\partial U_i}\right)\delta U_i - \sum_{k,k\neq l}\frac{\partial F}{\partial U_k}\delta U_k - \frac{\partial F}{\partial U_l}\delta U_l = \sum_k F^n + JS_t^n. \qquad (73)$$

An implicit relation is then established between the ghost data and the physical data in the interior. This is achieved by constructing a matrix, C, where

$$\delta U_l = C\delta U_i. \qquad (74)$$

Substituting $C\delta U_i$ into (73) eliminates node l from the set of equations, leaving the boundary flux determined implicitly in terms of the interior nodes and the specified relation (74). For example, at an adiabatic wall, $C = \text{Diag}[1, -1, -1, -1, 1, ...]$, whilst for a supersonic inlet or outlet, $C = \alpha I$, where $\alpha = 0$ or 1, respectively. Symmetry, subsonic inlet/outlet and isothermal wall boundary conditions are slightly more involved, since C becomes less sparse, but otherwise these boundaries are treated in an identical fashion. Higher-order boundary conditions can be implemented by deriving an implicit relation between the ghost node and two or more interior nodes.

The solution to the resulting system of equations is obtained via line-relaxation, using Chakravarthy's block-tridiagonal solver, NBTRIP (see the appendix of [2]).

To minimise storage, the Jacobians are recomputed line-by-line as needed. Since the construction of the Jacobians and the block-inversion routine is quite costly, an accurate solution of the linearised system is not attempted. Instead, only one sweep through each set of coordinate lines is performed at each time step. The CFL number is typically increased from an initial value close to unity at a rate of around 1.2 per step.

5. RESULTS AND CONVERGENCE HISTORIES

5.1. *Rationale for Selected Test Cases*

The main aim of the paper has been to devise implicit methods suitable for steady laminar or quasi-steady turbulent viscous flow. Whilst it has been argued that the property of exact resolution of contact and shear waves is important in viscous flow, the schemes which exhibit this property tend to be the most expensive to implement. It is instructive, therefore, to examine the various possible approaches with regard to accuracy, convergence rate and overall CPU cost.

The schemes are applied to five test cases, namely: subsonic and supersonic inviscid channel flow, low speed flow over a sphere, high-speed flow over a cylinder, and turbulent, transonic flow in a channel. These cases together feature a wide range of physical conditions, including massive subsonic separation, shock reflection, shock/boundary-layer interaction, and strong, curved bow shocks provoked by cylindrical obstructions in hypersonic flow.

5.2. *Supersonic Channel Flow*

The first example is that of inviscid flow at Mach 1.4 over a 4% circular arc bump in a channel (Fig. 9). The mesh used was 90×30, and the residual was taken throughout as the normalised flux-imbalance sum of the u-momentum equation. A constant CFL number of one million was used in all cases, except in those deferred-correction calculations which used the fully linearised Roe and HLLC fluxes. These calculations were found to be unstable at very large *initial* CFL numbers. Therefore, in these two cases, the CFL number was raised from 10^2 to 10^6 at a rate of 1.2 per iteration.

Figure 10 shows convergence histories computed with the first-order upwind schemes using backward Euler time-stepping. This can be considered as a Newton method for the fully linearised flux schemes. Despite using just a single alternating line-relaxation sweep, all schemes exhibit a rapid convergence to 10^{-10}. Both the fully linearised schemes converge slightly faster than the simplified frozen Jacobian Roe scheme and frozen acoustic wave speed HLLC scheme. Although the fully linearised Roe scheme converges faster than the frozen Jacobian scheme, the cost per iteration of the former outweighs the savings gained by the reduction in the number of iterations. It is interesting to note the closely similar convergence histories obtained by both fully linearised Roe and HLLC schemes (left plot in Fig. 10).

Figure 11 shows convergence histories for the same case using the various higher-order, deferred-correction schemes. Again, the fully linearised forms show an im-

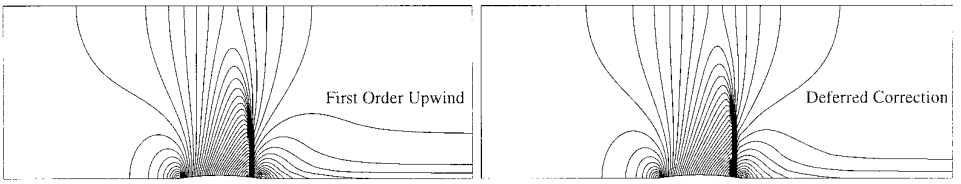

FIG. 14. Mach contours for Mach 0.85 circular-arc bump flow (HLLC).

proved convergence rate, but this does not have a significant impact on the overall CPU time required. The fully linearised Roe scheme is amongst the slowest of the schemes examined with respect to CPU time, despite having one of the fastest convergence rates. The implicit HLL scheme requires almost double the number of iterations used by the HLLC/Roe schemes, whilst the Rusanov scheme fails to depress the residuals below 10^{-6}.

5.3. *Subsonic Channel Flow*

Figures 14 to 16 show results for the GAMM test case of inviscid subsonic flow at Mach 0.85 over a 4.2% circular-arc bump in a channel with height 2.073 times the chord length. The mesh used was 99×34, and a constant CFL number of 50 was adopted in all cases. In both first- and second-order calculations, the frozen-Jacobian Roe scheme required the least number of iterations, and its convergence in terms of overall CPU time was almost identical to the frozen acoustic-speed HLLC scheme. The fully linearised form of Roe's scheme again showed no overall advantage, despite its rapid convergence rate. For the higher-order calculations (see Fig. 16), the fully linearised HLLC scheme was, overall, slightly slower than the simplified HLLC and Roe schemes. The Rusanov scheme displays a smoother convergence history than HLL, probably due to the damping of the upstream-moving acoustic waves. This feature sometimes helps improve convergence, but also causes the Rusanov scheme to give poorer resolution of stationary shock waves.

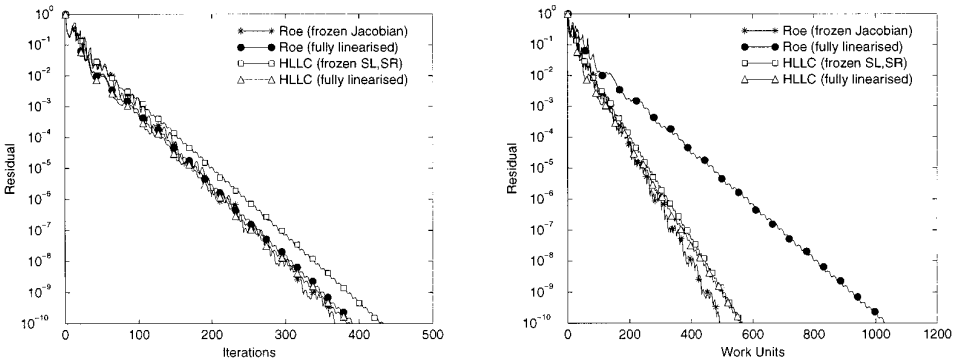

FIG. 15. Convergence histories of first-order backward Euler schemes on subsonic bump flow.

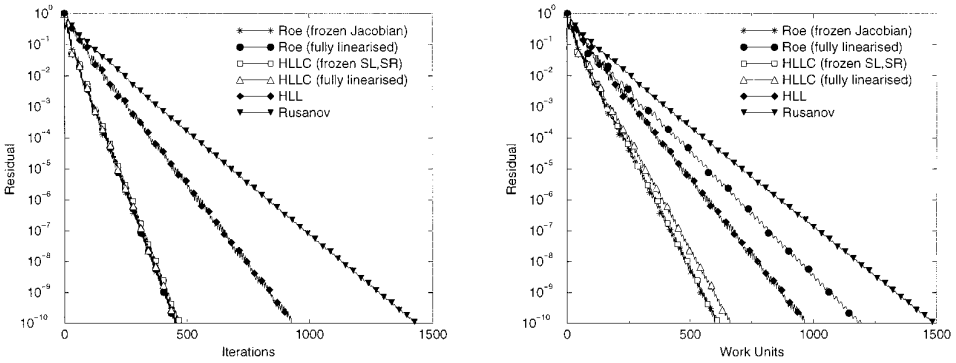

FIG. 16. Convergence histories of deferred correction B2 schemes on subsonic bump flow.

5.4. *Low-Speed Flow over a Sphere*

Figures 17 to 19 show results for the flow over a sphere at various Reynolds numbers. All these flows are essentially incompressible and were therefore solved at Mach 0.2, using B2 time-stepping with a constant local time-step corresponding to an inviscid CFL number of 200 in each cell (the backward Euler scheme failed to converge by even one order of magnitude at these conditions). The term "inviscid CFL number" here implies that the time-step is constrained only by the mesh-spacing and the fastest acoustic velocity. Source term and viscosity effects are not included in the calculation of the time-step, as such restrictions are not found necessary for the stability of the present implicit scheme.

A grid composed of $128 \times 200 \times 2$ mesh points was generated by rotating a clustered two-dimensional mesh through a small angle, $\theta = 10^{-2}$ Radians. This resulted in a wedge-shaped three-dimensional mesh, in which symmetry conditions

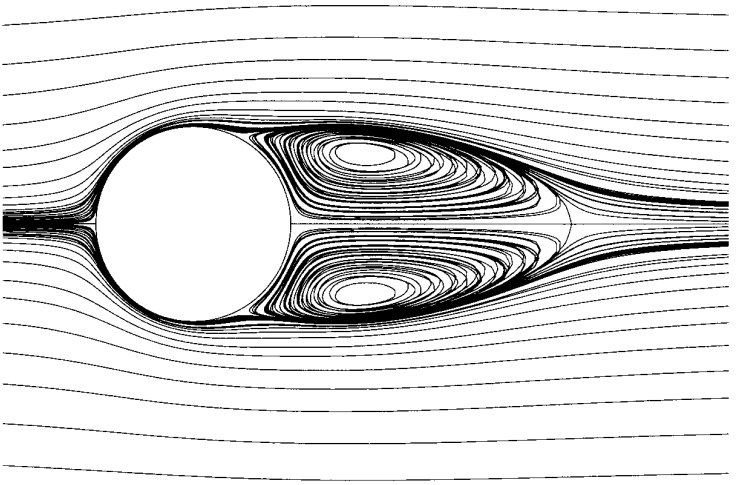

FIG. 17. Particle traces for sphere flow at Reynolds number 200.

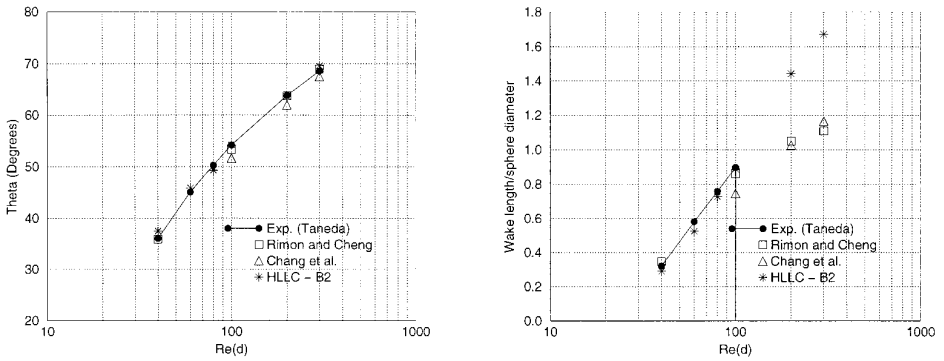

FIG. 18. Separation angle (left) and wake length (right) versus Reynolds number for low-speed sphere flow.

were imposed on its two azimuthal faces. The symmetry axis implies zero flux on the lower boundary, since the area of the cell face normal to the axis vanishes on the axis itself. The surface of the sphere was taken as an adiabatic wall boundary. At the outer boundary, 37 radii removed from the centre of the sphere, a general boundary procedure was used, in which either Riemann invariant subsonic-inflow boundary conditions or fixed back-pressure outflow boundary conditions were imposed, according to the local characteristic count at that boundary. All boundary conditions, including the symmetry boundaries on the sides of the wedge, were treated implicitly.

Figure 17 shows particle traces obtained from the HLLC solution of the sphere flow at a Reynolds number of 200. Figure 18 shows the present predictions of wake-length and separation angle, measured in degrees around the sphere. Up to a Reynolds number of 100, good agreement is obtained between the predictions of the present HLLC scheme, the predictions of Rimon and Cheng [29], and the experimental results of Taneda, also given in [29]. The predictions obtained with the HLLC, exact Riemann solver, and Roe fluxes were identical to at least two significant digits for all cases. The HLL and Rusanov schemes predicted a marginal decrease in the wake length (not shown). The separation angles computed by Chang *et al.* [5] show a slight deviation from the other three results in Fig. 18. According to Taneda [29], a Reynolds number of 130 is roughly the point at which the wake becomes unsteady. There are therefore no experimental data available for the wake length above this Reynolds number, and for these cases there is a significant deviation amongst the computed predictions. The present computations cannot, of course, resolve unsteady shedding because of the axi-symmetry condition imposed.

Figure 19 shows the convergence histories for the flow at Reynolds number 200, using the various implicit schemes. At these low Reynolds numbers, all schemes which exactly preserve isolated contact/shear-waves display closely similar convergence rates, probably because the convergence is dominated by the (identical) implicit treatment of the viscous terms. The scheme with frozen acoustic wave speeds HLLC converges in just one iteration less than the frozen-Jacobian Roe

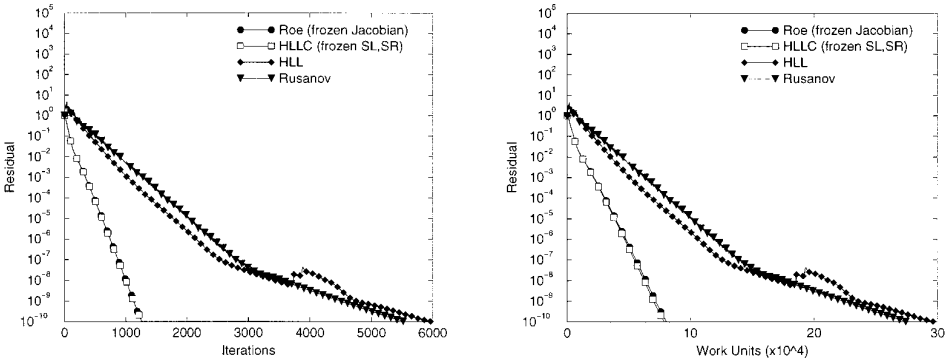

FIG. 19. Convergence histories of deferred correction B2 schemes on sphere flow at Re = 200.

scheme. The HLL and Rusanov schemes both take significantly longer to converge, both in terms of iterations and overall CPU time.

5.5. *Hypersonic Flow over a Circular Cylinder*

Figures 20 to 22 show computations of a Mach 5.7 flow over a circular cylinder at Reynolds number 16500, based on cylinder diameter, and total temperature and pressure of 300K and 95KPa, respectively. Experimental results produced by McCarthy and Kubota [23] suggest that the flow, including the wake, is laminar at these conditions; hence, no turbulence model was employed in the calculations. The flow was treated as a perfect gas and computed over the full cylinder, with no imposed symmetries.

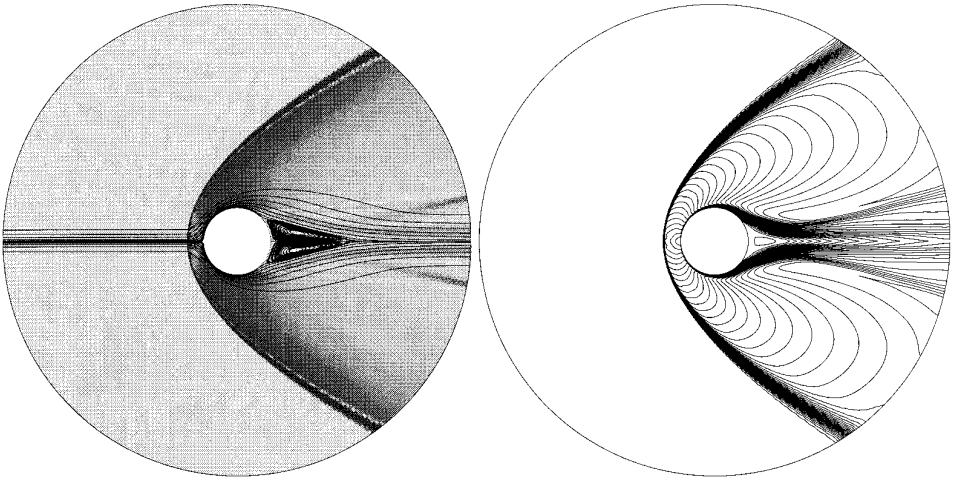

FIG. 20. Hypersonic cylinder flow. Schlieren image showing particle traces computed with deferred correction HLLC scheme on 480 × 200 mesh (left) and Mach contours computed with first-order HLLC scheme on 240 × 200 mesh (right).

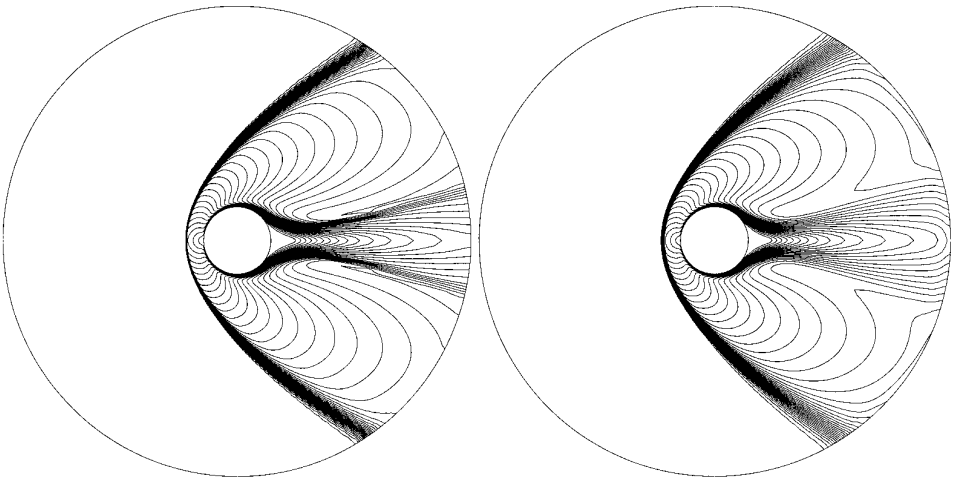

FIG. 21. Hypersonic cylinder flow. Mach contours computed with first-order HLL scheme (left), and Rusanov scheme (right) using 240 × 200 mesh.

The mesh comprised of 240 points in the circumferential and 200 points in the radial directions, and the outer boundary, also treated via a general implicit condition based on the locally computed characteristics, was placed at seven radii away from the centre of the cylinder. The CFL number was raised from 1.0 to 10^6 at a rate of 1.02 per step. All deferred-correction schemes failed to converge more than two orders of magnitude on this test case. Convergence of the higher-order schemes also stalled on a 480 × 200 grid, and there may be some question as to whether the wake is truly steady. The convergence histories presented for this case were all computed using the first-order upwind schemes, although results of a second-order computation on a 480 × 200 mesh are also shown. This case proved an exception to the generally observed convergence trends, with the most diffusive scheme (Rusanov) displaying a convergence rate almost as rapid as that of HLLC and requiring the least overall CPU time.

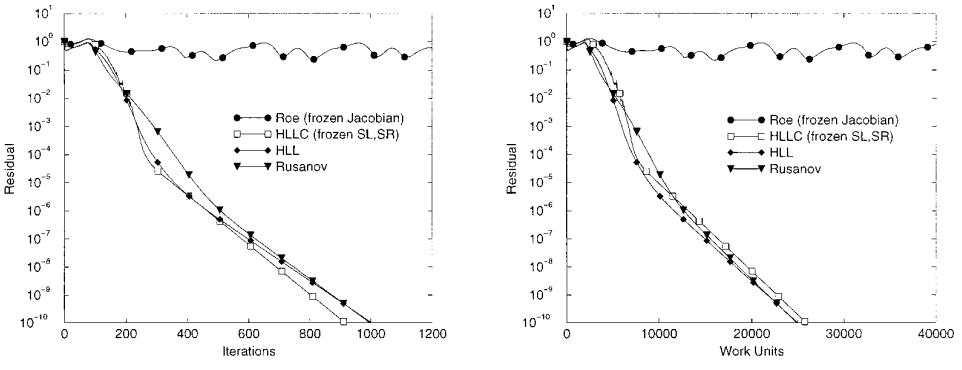

FIG. 22. Convergence histories of first-order B2 schemes on hypersonic cylinder flow.

Despite the gradually increased CFL number, Roe's scheme failed in the first few steps, giving negative pressures in the wake. This occurred for arbitrarily small CFL numbers, and it therefore proved necessary to clip these negative pressures and densities to some small positive value (see Yee *et al.* [40]). It was further found necessary to restrict the local CFL number in the Roe scheme to about 3 to prevent the solution from diverging. Even at a maximum local CFL number of 3, the Roe scheme failed to converge and produced a carbuncle on the bow shock which pulsated indefinitely at a regular frequency.

Whilst certain problems with Roe's scheme, such as the generation of expansion shocks and negative pressures, can be traced directly to inappropriate physical modelling (i.e., the underestimation of the true expansion-wave velocity), it is still basically unclear why Roe's scheme suffers so badly from the above type of instability. Note that both the HLLC and unmodified Roe schemes represent the internal structure of the Riemann fan as two integral-average states, and both share the property of the exact Riemann solver of isolated discontinuities being preserved exactly. We do not believe, therefore, that this effect is due to any lower levels of dissipation or greater accuracy in Roe's scheme. The results computed with an exact Riemann solver (not shown) did not exhibit this pulsating-carbuncle effect and were indistinguishable from the results computed with the HLLC scheme. The solutions generated with Roe's scheme were observed to be sensitive to CFL, grid, and also initial conditions. Hence, it is possible that this pulsation could be avoided by suitably adjusting one or all of these numerical parameters. Alternatively, entropy corrections can be employed in Roe's scheme which involve modifying the linear eigenvalue to be some function of the maximum modulus eigenvalue (see, for example, Yee *et al.* [40]). This correction is, in effect, just a convenient way of adding extra artificial viscosity to Roe's scheme and has no physical justification. Such a modification to the linear eigenvalue will destroy the conservation property of fluctuation-splitting schemes [31] and will also destroy the ability of any linearised scheme to exactly preserve isolated contact and shear waves. In addition to introducing artificial diffusion through boundary layers, this deficiency has been shown here to delay convergence of implicit schemes, even in inviscid flow.

5.6. *Transonic Turbulent Flow over a Bump*

This test case involves turbulent shock-induced separation in a transonic flow over a bump in a channel (Délery [8, case C]). In the experiments, high-pressure gas was supplied through a reservoir upstream, and the shock position was controlled by an adjustable throat downstream of the bump. In the present computations, we follow earlier calculations in the European Validation Exercise for Aerodynamic Flows [13] in adjusting the shock location by controlling the back-pressure on the outflow boundary. The inlet boundary condition was treated by assuming a fully developed turbulent boundary layer on both upper and lower walls of the channel. The flow properties through the boundary layer were specified by imposing a Musker profile, corrected for compressibility effects [12], such that both boundary layers were 3% of the channel height at the inlet. These quantities were used to specify the inlet conditions needed for the Riemann invariant subsonic-inflow

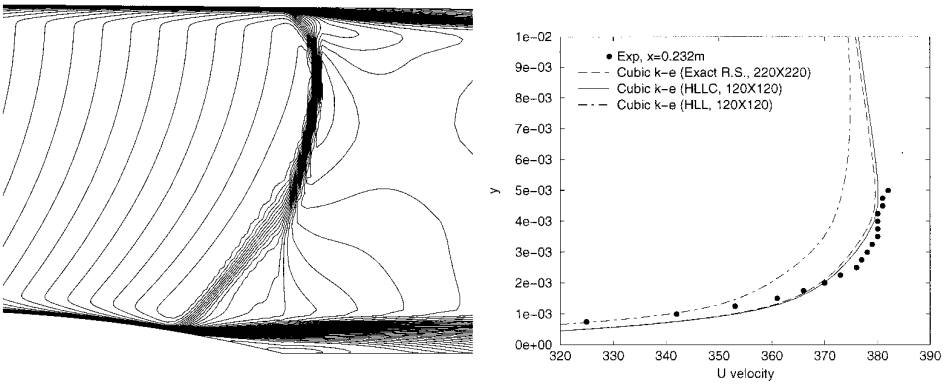

FIG. 23. Délery's case C—Mach contours showing close-up of shock/boundary-layer interaction region computed with HLLC scheme and cubic eddy-viscosity model (left) and boundary-layer velocity profiles upstream of the interaction region, $x = 0.232$ m (right).

procedure. Alternatively, this case may be run using reservoir inlet conditions, in which only the total pressure and temperature are specified, and the velocity profile at the inlet is allowed to develop as part of the solution. Due to the rapid acceleration of the flow over the bump, the two approaches do not result in significant differences in the thickness of the boundary layer just prior to the shock-interaction region, and no major differences have been observed between the two types of inflow-boundary treatment. The stagnation pressure and temperature in the plenum were 96 KPa and 300 K, respectively, and the back pressure was fixed at 91 KPa for all cases. This results in an incoming Mach number of about 0.615 and a Reynolds number of approximately 10^7 per metre. Extensive details of this test case may be found in Loyau and Vandromme's summary of the ETMA workshop [22] and in Leschziner *et al.* [19].

A 120×120 grid was used, with grid independence being confirmed by further computations on a 220×220 grid. Both grids were clustered to give $y^+ \leq 0.5$ for the first cell-centroids off both walls resulting in cell-aspect ratios on the 120×120 mesh ranging from about 500 near the interaction region, to around 6000 near the inflow boundary. All computations were carried out using the deferred-correction scheme with van Leer's limiter, at an inviscid CFL number that was increased from 1 to 100 at a rate of 1.2 per iteration. The turbulence model used was the low-Reynolds-number, nonlinear (cubic) eddy-viscosity model proposed by Lien *et al.* [20], which gives, in incompressible separated flow, results that are superior to linear k-ε models.

This flow is characterised by a strong acceleration to supersonic conditions, followed by a deceleration through a lambda-shock structure on the trailing edge of the bump. This feature is just visible in the left plot of Fig. 23. The initial impingement of the shock wave on the boundary layer induces an extended separation region behind the bump, effectively displacing the downstream boundary layer and strengthening the second leg of the lambda-shock where the flow finally decelerates to subsonic conditions. The separation bubble gives rise to the characteristic pressure

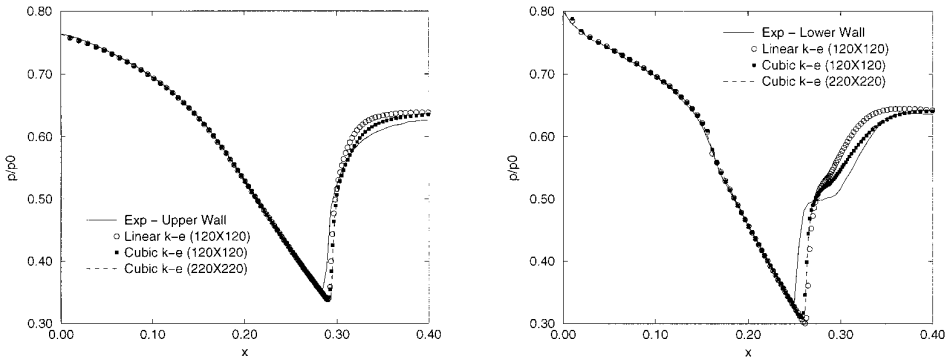

FIG. 24. Wall-pressure distributions for Dèlery's case C.

plateau shown by the experimental data on the right plot of Fig. 24. Although there are some discrepancies between experiment and all calculations, the nonlinear eddy-viscosity model shows better agreement than a conventional linear eddy-viscosity model, which is here the model of Launder and Sharma [18], held to be the best low-Reynolds-number k-ε linear variant.

The difference in the level of numerical diffusion for the same 120×120 mesh is apparent in the right plot of Fig. 23, where the HLL scheme shows a noticeably thicker boundary-layer profile (similar observations apply to the Rusanov flux). In turn, this affects turbulence generation near the wall, resulting in lower levels of eddy viscosity in the shear layer, fortuitously compensated by an excessive artificial dissipation. In theory, the HLL and Rusanov results ought to improve with the addition of more mesh points normal to the wall and/or the use of a more compressive limiter. However, even with the B2 time-stepping, both schemes here failed to reduce the residual by even one order of magnitude (see Fig. 25).

The contamination of boundary layers by artificial dissipation was recognised in artificial-viscosity schemes [1, 24] and early flux-vector splitting schemes [35], none of which could preserve isolated contacts or shear waves. The fact that certain

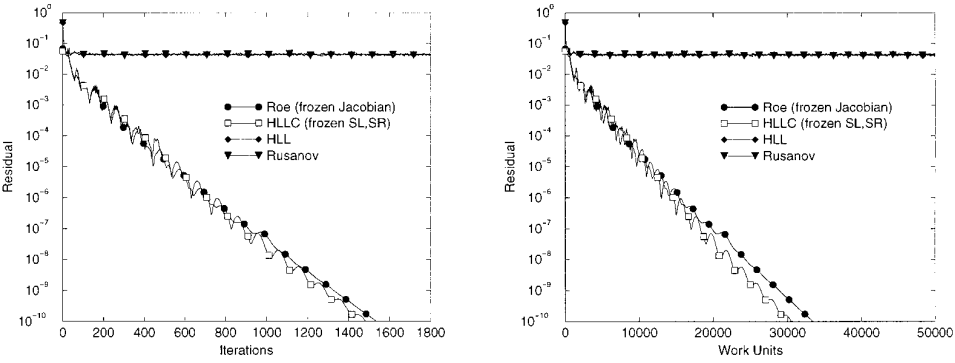

FIG. 25. Convergence histories for Délery's case C.

schemes ignore the contact wave in their explicit formulations, implies that the corresponding details must also be missing from their Jacobians. These waves will not, therefore, be correctly propagated at Courant numbers larger than unity, and the consequences are excessive dissipation of boundary layers and delayed convergence. A further difficulty is encountered when turbulence-transport models are employed. The additional transport equations rely on the convective-flux model to faithfully carry the turbulence parameters from the inlet to the point at which the local flow physics becomes dominated by production, dissipation, or diffusion through the shear-layer. The omission of the contact wave means an inaccurate transport of the turbulence quantities. Although remedies may be devised—based, for example, on artificially reducing dissipation via user-tunable parameters or modified flux models for transported scalars—the general benefit of such an approach is uncertain and potentially costly.

6. CONCLUSIONS

A number of new implicit schemes based on average-state flux Jacobians have been proposed. The convergence histories of these implicit schemes consistently show an improved convergence rate when more physical detail of the Riemann fan is included in the closed-form approximation to the flux and its Jacobian. This is not an entirely obvious conclusion, since one might have expected simple closed-form approximate solutions to converge (albeit to a less accurate solution) in less CPU time, purely by virtue of the reduced number of floating-point operations. Our experience suggests this is generally not the case. The schemes containing more detailed physics not only give more accurate solutions, but also tend to yield faster overall convergence.

The convergence rates of the HLLC scheme with frozen acoustic wave speeds and the frozen Jacobian Roe scheme are closely comparable. The slight differences that do arise are attributed to the different approximations which have been made to simplify the Jacobians. These differences are necessitated by the very different construction of the two methods. Although there is no dramatic difference in CPU times between the two simplified forms, the fully linearised HLLC scheme is faster by at least a factor of two (per iteration) relative to the fully linearised Roe scheme. This might be significant for Newton-type methods, since both fully linearised schemes display an otherwise closely similar convergence rate.

It has been shown that the space-time and FORCE schemes can be considered as average-state schemes on nonstaggered meshes using a particular flux which was named ''HLF.'' However, the HLF scheme is not practical for use in an implicit method, as it is not bounded above a CFL number of 0.5. A similar CFL restriction is expected to carry over to implicit FORCE and space-time schemes. The HLF, FORCE, and space-time schemes are remarkably accurate for explicit calculations of the unsteady Euler equations, but none appears well-suited to Navier–Stokes computations because none can exactly preserve isolated contacts or shear waves. Although the underlying monotone method in the space-time scheme can be considered as being at the lower end of the current Riemann-solver hierarchy, the method of obtaining higher-order accuracy developed by Chang [6] appears to be superior

to most existing two-step explicit, co-located-storage MUSCL schemes and may be worth pursuing further.

The property of exact preservation of isolated contact and shear waves has been argued to be an important attribute of a convective-flux model. This property prevents contamination of the boundary layer via artificial diffusion and also leads to improved convergence rates of implicit schemes, even in inviscid flow. The exact Riemann solver, HLLC, and (unmodified) Roe fluxes are all capable of preserving isolated discontinuities exactly, and all should be capable of giving respectable solutions to laminar and turbulent viscous-flow problems. However, no entropy correction was included in the present calculations using the implicit Roe scheme, and this unmodified Roe scheme is clearly not satisfactory. Some form of correction would be required, in general, but this would be likely to increase both the required number of iterations and the overall CPU time.

Due to the positivity-preserving property of the HLLC flux [4] and the fact that the entropy condition is strongly enforced without the need for additional modifications, the implicit HLLC scheme would seem to be a promising method for compressible viscous flow. It should be noted that positivity-preservation will not be guaranteed for any of these implicit schemes (even first-order upwind variants) operating at an infinite time step, because interacting waves may create signal velocities larger than those estimated in the initial computation of the fluxes and their respective Jacobians. In practice, if one marches gradually towards an infinite CFL number, there is some evidence that these average-state schemes will be more robust than conventional, linearised implicit schemes which can fail well within the explicit CFL limit.

In view of the improved accuracy and reduced CPU time displayed by the more sophisticated one-dimensional flux models, further improvement might be anticipated from the use of genuinely multidimensional upwind schemes, particularly in situations where shear layers or wakes are not well aligned with the grid. The fluctuation-splitting approach (based on a reformulation of Roe's linearised upwind scheme [31]) appears to be the simplest route currently available to achieving genuinely multidimensional upwind methods [26]. It is rather unfortunate that this approach tends to be amongst the least reliable of existing one-dimensional/grid-aligned upwind methods. A genuinely multidimensional, positively conservative scheme for nonlinear systems continues, therefore, to be an elusive goal.

ACKNOWLEDGMENTS

The authors thank Professor George Huang, of the University of Kentucky, for a number of useful communications. The financial support of British Aerospace is gratefully acknowledged.

REFERENCES

1. S. R. Allmaras, Contamination of laminar boundary layers by artificial dissipation in Navier–Stokes solutions, in *Proceedings, ICFD Conference, University of Reading, 1992.*
2. D. Anderson, J. C. Tannehill, and R. H. Pletcher, *Computational Fluid Mechanics and Heat Transfer* (Hemisphere, Washington, DC, 1986).

3. G. Barakos and D. Drikakis, Implicit-coupled implementation of two-equation turbulence models in compressible Navier–Stokes methods, *Int. J. Numer. Methods Fluids,* submitted.
4. P. Batten, N. Clarke, C. Lambert, and D. M. Causon, On the choice of wave speeds for the HLLC Riemann solver, *SIAM J. Sci. Stat. Comput.* **18**(6), (1997).
5. C-C. Chang, B-H. Liou, and R-Y. Chern, An analytical and numerical study of axisymmetric flow around spheroids, *J. Fluid Mech.* **234,** 219 (1992).
6. S. C. Chang, The method of space-time conservation element and solution element—A new approach for solving the Navier–Stokes and Euler equations, *J. Comput. Phys.* **191,** 295 (1995).
7. S. F. Davis, Simplified Second-Order Godunov-Type Methods. *SIAM Journal on Scientific and Statistical Computing,* **9**(3), (1988).
8. J. M. Délery, Experimental Investigation of Turbulence Properties in Transonic Shock-wave/Boundary-Layer Interactions. *AIAA J.* **21,** 180 (1983).
9. A. Eberle, Characteristic Flux Averaging Approach to the Solution of Eulers Equations. In *VKI Lecture Series 1987-04* (Vestnik, Kièv, 1987).
10. B. Einfeldt, C. D. Munz, P. L. Roe, and B. Sjogreen. On Godunov-Type Methods Near Low Densities. *J. Comput. Phys.* **92,** 273 (1991).
11. S. K. Godunov. A Difference Method for the Numerical Calculation of Discontinuous Solutions of Hydrodynamic Equations. *Mat. Sb. 47,* 271, (1959).
12. U. C. Goldberg. Exploring a 3 Equation R-k-ε Turbulence Model. *ASME J. Fluid Mech.* **12** (1996).
13. W. Haase, F. Brandsma, E. Elsholz, M. A. Leschziner, and D. Schwamborn (Es.), *EUROVAL—A European Initiative on Validation of CFD Codes* (Vieweg, Viesbaden, 1993).
14. A. Harten, P. D. Lax, and B. Van Leer, On Upstream Differencing and Godunov-Type Schemes for Hyperbolic Conservation Laws. *SIAM Review,* **25**(1), 35 (1983).
15. P. G. Huang and T. J. Coakley, An implicit Navier–Stokes code for turbulent flow modeling, AIAA Paper 92-0547, 1992.
16. A. Jameson, Numerical Solution of the Euler Equations for Compressible Inviscid Fluids, in *Proc. INRIA Workshop on Numerical Methods for the Euler Equations of Fluid Dynamics* (SIAM, Philadelphia, 1985).
17. A. Jameson, Artificial Diffusion, Upwind Biasing, Limiters and their Effect on Accuracy and Multigrid Convergence in Transonic and Hypersonic Flows. *AIAA Paper 93-3359,* 1993.
18. B. E. Launder and B. I. Sharma, Application of the Energy-Dissipation Model of Turbulence to the Calculation of Flow Near a Spinning Disc. *Lett. Heat Mass Transfer* **1,** 131 (1974).
19. M. A. Leschziner, K. P. Dimitriadis, and G. Page, Computational modelling of shock wave/boundary layer interaction with a cell-vertex scheme and transport models of turbulence, *Aeronaut. J.* February (1993).
20. F-S. Lien, W. L. Chen, and M. A. Leschziner, Low-Reynolds-Number Eddy-Viscosity Modelling Based on Non-Linear Stress-Strain/Vorticity Relations, in *3rd Symp. on Engineering Turbulence Modelling and Measurements, Crete, Greece, 1996.*
21. M-S. Liou and C. J. Steffen Jr., A new flux splitting scheme, *J. Comput. Phys.* **107,** 23 (1993).
22. H. Loyau and D. Vandromme, TC5 Workshop Synthesis. In *Proc. of ETMA Workshop, UMIST, Manchester, 1994.*
23. J. F. McCarthy and T. Kubota, A Study of Wakes Behind a Circular Cylinder at M = 5.7. *AIAA Journal,* **2**(4), 629 (1964).
24. C. Y. McNeil, The Effect of Numerical Dissipation on High Reynolds Number Turbulent Flow Solutions, in *34th Aerospace Sciences Meeting, Reno, Nevada, 1996.* [*AIAA Paper 96-0891*].
25. C. D. Munz, R. Schneider, M. Goz, and A. Herschel, Study of numerical approximations of gas flow into vacuum, technical report, University of Karlsruhe, 1993.
26. H. Paillere, H. Deconick, and E. van der Weide, Upwind residual distribution schemes for compressible flow: An alternative to finite volume and finite element methods, in *VKI L-S 1997-02,* (Vestnik, Kiev, 1997).

27. S. V. Patankar, *Numerical Heat Transfer and Fluid Flow* (Hemisphere, Washington, DC, 1980).
28. J. J. Quirk, *A Contribution to the Great Riemann Solver Debate,* Technical Report ICASE TR 92-64, 1992.
29. Y. Rimon and S. I. Cheng, Numerical Solution of a Uniform Flow over a Sphere at Intermediate Reynolds Numbers, *Physics of Fluids,* **12**(5), (1969).
30. P. L. Roe, Approximate Riemann Solvers, Parameter Vectors and Difference Schemes, *Journal of Computational Physics Vol. 43,* 357, (1981).
31. P. L. Roe and J. Pike, Efficient Construction and Utilisation of Approximate Riemann Solutions. In *Proceedings of IMA conference on numerical methods in fluid dynamics, Computing Methods in Science and Engineering VI, North-Holland, INRIA, 1984.*
32. E. F. Toro, A Linearised Riemann Solver for the Time-Dependent Euler Equations of Gas Dynamics, *Proc. Royal Society Lond. (A)* **434,** 683 (1991).
33. E. F. Toro, *On Glimm Related Schemes for Conservation Laws,* Manchester Metropolitan University Technical Report TR-9602, 1996.
34. E. F. Toro, M. Spruce, and W. Speares, Restoration of the contact surface in the HLL Riemann solver, *Shock Waves* **4,** 25 (1994).
35. B. van Leer, J. L. Thomas, P. L. Roe, and R. W. Newsome, A comparison of numerical flux formulas for the Euler and Navier–Stokes equations, *AIAA 87-1184,* 1987.
36. H. C. Yee, Linearized form of implicit TVD schemes for the multidimensional Euler and Navier–Stokes equations, *Comput. & Math. App. A***12**(4/5), 413 (1986).
37. H. C. Yee, Construction of Explicit and Implicit Symmetric TVD Schemes and their Applications. *J. Comput. Phys.* **68**(1), 151 (1987).
38. H. C. Yee, *A Class of Explicit and Implicit Shock Capturing Methods,* NASA Technical Report TM 101088, 1989.
39. H. C. Yee, *Explicit and Implicit Compact High Resolution Shock-Capturing Methods for Multidimensional Euler Equations 1: Formulation,* NASA Technical Report TM 110364, 1995.
40. H. C. Yee, G. H. Klopfer, and J.-L. Montagne, High resolution shock-capturing schemes for inviscid and viscous hypersonic flows, *J. Comput. Phys.* **88**(1), (1990).
41. H. C. Yee and P. K. Sweby, *Numerical Dynamics & Numerical Uncertainties in CFD,* NASA Technical Report TM 110398, 1996.